Designing and prototyping of a transverse flux machine in soft magnetic composite using milling and turning techniques

Master's thesis in Electrical power engineering

FELIX MANNERHAGEN

Designing and prototyping of a transverse flux machine in soft magnetic composite using milling and turning techniques

FELIX MANNERHAGEN

Designing and prototyping of a transverse flux machine in soft magnetic composite using milling and turning techniques
FELIX MANNERHAGEN

Designing and prototyping of a transverse flux machine in soft magnetic composite using milling and turning techniques
Master's thesis in Electrical power engineering
FELIX MANNERHAGEN
Electric Power Engineering at Energy and Environment
Chalmers University of Technology

Abstract

In this thesis a polyphase claw pole machine has been designed, prototyped and verified through measurements. The FE-calculation model have been verified against analytical calculations, there after the design have been changed through an iterative process to a more optimised design. The machine have then been built in a soft magnetic composite, using milling and turning techniques. The techniques used to minimise the chapped edges is described. The FE-calculated machine model is then verified against equal circuit parameters measurements, with a relative small error.

Keywords: Claw pole, transverse flux, electrical machine design, SMC, soft magnetic composite, prototyping, milling, turning

Preface

Acknowledgements

CONTENTS

1 Introduction

With the electrification of the automotive fleet, the demand on rare earth magnets has increased, since the most utilised type of machines for propulsion are permanent magnet machines which today use relatively large volumes of neodymium for the magnets. Since neodymium is mainly mined in bad conditions [1], the increasing usage of rare earth materials may be harmful to the environment [2], as well as to the health of the mine worker. One way to lowering the need for rare earth magnets could be to utilise the reluctance torque in salient machines.

The electrical machine should be designed with the constraints to fit in a small single person transportation vehicle, like a moped. The machine should be designed to deliver around 1 hp or 750 W at a rated speed of around 2500 rpm. The peak burst torque should be around 15 Nm with a peak power output of 2 hp or 1500 W. The system voltage of the drivetrain should be 48 V. The length constraint of the machine is that it should be shorter then 70 mm.

The machinability of soft magnetic composites has come a long way, which gives new possibilities for more complex geometries in electrical machine design. Larger fillets, larger cutout and thinner structures should be possible with the soft magnetic composite materials available today.

This thesis should deliver an understanding in the possibilities of electrical machines designs and the prototyping limitations in soft magnetic composite materials. The claw pole design should give the possibilities for simpler winding structure without end-windings which gives the possibility to have a shorter machine. The claw pole design could be a cheap alternative in that manufacturing step compared to other machine topologies.

1.1 Accuracy description in text

All value accuracy shown in this thesis is written as Significant figures. Accuracy in analytical calculations is set from rounding errors. The accuracy in FE-calculation is derived from convergence dependency from the mesh refinement. Accuracy in measurements is set from the accuracy in the measurements setup.

1.2 Environmental aspect

When sintering electromagnetic components from iron power, as is done in soft magnetic composites, there is low to non waste of material, since the excess powder can be reused in the next part [3]. The recycling of materials from parts made of soft magnetic composites is a fairly known process [4]. The part is crushed and the soft magnetic material is removed utilising the magnetic properties while the copper windings remain [5].

2   Electromagnetic theory

This section starts with the mathematical explanation of the dq-transform, the mathematical differentiation of magnetic and reluctance torque and how the dq-currents can be used to control the machine. The machine topology is briefly explained and some of the limitations of the manufacturing is presented. The section then ends with the theory used in the verification of the FE calculations.

2.1   Mathematical backround

To be able to get the mathematical description of the machine in a more familiar form the dq-transform will be used. This subsection will go through the steps taken to derive the dq-parameters later used to design and verify the claw pole machine. The voltages in the 3-phase system are expressed as

$$
\begin{aligned}
u_a &= R_a i_a + \frac{\mathrm{d}\Psi_a}{\mathrm{d}t} \\
u_b &= R_b i_b + \frac{\mathrm{d}\Psi_b}{\mathrm{d}t} \\
u_c &= R_c i_c + \frac{\mathrm{d}\Psi_c}{\mathrm{d}t}
\end{aligned}
\tag{2.1}
$$

The self-inductance of the stator windings is approximated as

$$
\begin{aligned}
l_{aa} &= L_{aa0} + L_{aa2}\cos(2\theta_r) \\
l_{bb} &= L_{aa0} + L_{aa2}\cos\left(2(\theta_r - 120°)\right) \\
l_{cc} &= L_{aa0} + L_{aa2}\cos\left(2(\theta_r + 120°)\right)
\end{aligned}
\tag{2.2}
$$

Where L_{aa0} is the average value of the self-inductance and L_{aa2} is the amplitude of the variations depending on rotor position. The mutual inductance between the stator windings is approximated as

$$
\begin{aligned}
l_{ab} = l_{ba} &= -\left(L_{ab0} + L_{aa2}\cos\left(2(\theta_r + 30°)\right)\right) \\
l_{bc} = l_{cb} &= -\left(L_{ab0} + L_{aa2}\cos\left(2(\theta_r - 90°)\right)\right) \\
l_{ca} = l_{ac} &= -\left(L_{ab0} + L_{aa2}\cos\left(2(\theta_r + 150°)\right)\right)
\end{aligned}
\tag{2.3}
$$

The flux linkage can then be expressed as

$$
\begin{aligned}
\Psi_a &= l_{aa}i_a + l_{ab}i_b + l_{ac}i_c + \Psi_m\cos(\theta_r) \\
\Psi_b &= l_{ba}i_a + l_{bb}i_b + l_{bc}i_c + \Psi_m\cos(\theta_r - 120°) \\
\Psi_c &= l_{ca}i_a + l_{cb}i_b + l_{cc}i_c + \Psi_m\cos(\theta_r + 120°)
\end{aligned}
\tag{2.4}
$$

If the assumption that there is no zero component in the 3-phase system is used, the flux

linkage can be written as

$$\Psi_a = \left(L_{aa0} + L_{ab0} + \frac{3}{2} L_{aa2} \cos(2\theta_r) \right) i_a$$

$$+ \frac{\sqrt{3}}{2} L_{aa2} \sin(2\theta_r)(i_b - i_c) + \Psi_m \cos(\theta_r)$$

$$\Psi_b = \left(L_{aa0} + L_{ab0} + \frac{3}{2} L_{aa2} \cos(2(\theta_r - 120°)) \right) i_b \tag{2.5}$$

$$+ \frac{\sqrt{3}}{2} L_{aa2} \sin(2(\theta_r - 120°))(i_c - i_a) + \Psi_m \cos(\theta_r - 120°)$$

$$\Psi_c = \left(L_{aa0} + L_{ab0} + \frac{3}{2} L_{aa2} \cos(2(\theta_r + 120°)) \right) i_c$$

$$+ \frac{\sqrt{3}}{2} L_{aa2} \sin(2(\theta_r + 120°))(i_a - i_b) + \Psi_m \cos(\theta_r + 120°)$$

The voltage can then be described in a two-phase system by

$$\bar{u}_s^s = u_{s\alpha} + j u_{s\beta} = \frac{2}{3}(u_a + u_b e^{j\frac{2\pi}{3}} + u_c e^{j\frac{4\pi}{3}}) \tag{2.6}$$

Equation (2.1) is then inserted in (2.6) which results in

$$\bar{u}_s^s = R_s \bar{i}_s^s + L \frac{\mathrm{d}\bar{\Psi}_s^s}{\mathrm{d}t} \tag{2.7}$$

where $\bar{\Psi}_s^s$ is described as

$$\bar{\Psi}_s^s = \frac{2}{3}(\Psi_a + \Psi_b e^{j\frac{2\pi}{3}} + \Psi_c e^{j\frac{4\pi}{3}}) \tag{2.8}$$

Equation (2.5) is then inserted in (2.8) and results in

$$\bar{\Psi}_s^s = \bar{L}_s \bar{i}_s^s + \Psi_m e^{j\theta_r} \tag{2.9}$$

where $\bar{\Psi}_s^s$ is the total flux linkage, $\bar{L}_s$ is the Leakage and mutual inductance and Ψ_m is the magnet flux linkage expressed in the αβ-system.

The rotation of the rotor is then added to the equations as

$$\bar{u}_s^s = \bar{u}_s e^{j\theta_r} \tag{2.10}$$

Equation (2.10) is then inserted in (2.7) and results in

$$\bar{u}_s e^{j\theta_r} = R_s \bar{i}_s^s e^{j\theta_r} + L \frac{\mathrm{d}\bar{\Psi}_s^s}{\mathrm{d}t} e^{j\theta_r} \tag{2.11}$$

The chain rule is applied on (2.11) and results in

$$\bar{u}_s e^{j\theta_r} = R_s \bar{i}_s^s e^{j\theta_r} + L \frac{\mathrm{d}\bar{\Psi}_s^s}{\mathrm{d}t} e^{j\theta_r} + j\omega_r \bar{\Psi}_s e^{j\theta_r} \tag{2.12}$$

The flux linkage from the rotational transformation looks like

$$\bar{\Psi}_s e^{j\theta_r} = (L_{aa0} + L_{ab0}) \bar{i}_s e^{j\theta_r} + \frac{3}{2} L_{aa2} e^{j(2\theta_r)} (\bar{i}_s e^{j\theta_r})^* + \Psi_m e^{j(\theta_r)} \tag{2.13}$$

3

which can be simplified to

$$\bar{\Psi}_s = (L_{aa0} + L_{ab0})\bar{i}_s + \frac{3}{2}L_{aa2}e^{j(2\theta_r - 2\theta_r)}\bar{i}_s^* + \Psi_m e^{j(\theta_r - \theta_r)} \tag{2.14}$$

Further simplified to

$$\bar{\Psi}_s = (L_{aa0} + L_{ab0})\bar{i}_s + \frac{3}{2}L_{aa2}\bar{i}_s^* + \Psi_m \tag{2.15}$$

By separating the complex current the flux linkage looks like

$$\bar{\Psi}_s = (L_{aa0} + L_{abo} + \frac{3}{2}L_{aa2})i_{sd} + (L_{aa0} + L_{abo} - \frac{3}{2}L_{aa2})i_{sq} + \Psi_m \tag{2.16}$$

were the complex inductance can be set to

$$L_{sd} = (L_{aa0} + L_{abo} + \frac{3}{2}L_{aa2})$$

$$L_{sq} = (L_{aa0} + L_{abo} - \frac{3}{2}L_{aa2})) \tag{2.17}$$

By inserting (2.17) in (2.16) the total flux linkage becomes

$$\bar{\Psi}_s = L_{sd}i_{sd} + jL_{sq}i_{sq} + \Psi_m \tag{2.18}$$

which inserted in (2.12) will result in

$$u_{sd} = R_s i_{sd} + L_{sd}\frac{\mathrm{d}i_{sd}}{\mathrm{d}t} - \omega_r L_{sq}i_{sq}$$

$$u_{sq} = R_s i_{sq} + L_{sq}\frac{\mathrm{d}i_{sq}}{\mathrm{d}t} + \omega_r L_{sd}i_{sd}\omega_r\Psi_m \tag{2.19}$$

which will describe the behavior of the permanent magnet machine with salient properties. From the equation system the equivalent circuit shown in Figure 2.1 is derived.
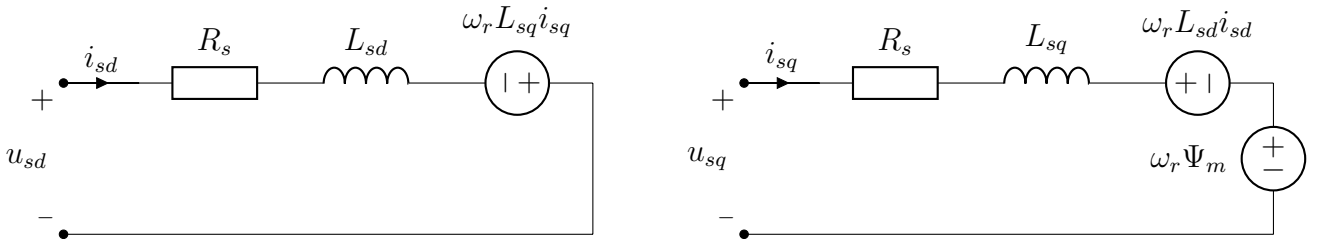

Figure 2.1: *Eqvivalent circuit model*

The shaft power can be calculated using

$$P_e = \frac{3\omega_r}{2} \cdot \mathrm{Im}\{\bar{\Psi}_s^* \bar{i}_s\} \tag{2.20}$$

where P_e is amplitude variant scaled. The torque can be calculated from

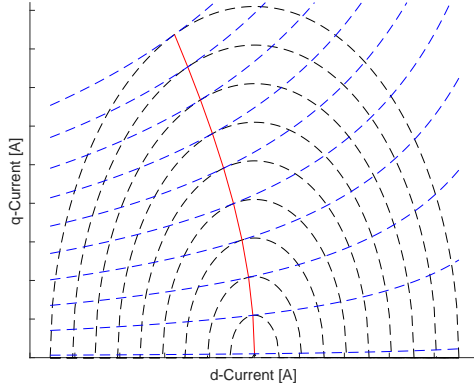$$T_e = \frac{3n_p}{2}(\Psi_m i_{sq} + (L_{sd} - L_{sq})i_{sd}i_{sq}) \tag{2.21}$$

4

Figure 2.2: *Example on a MTPA curve*

where the torque produced from the magnet is

$$T_m = \frac{3n_p}{2}(\Psi_m i_{sq}) \tag{2.22}$$

and the torque produced from the salient properties is

$$T_r = \frac{3n_p}{2}((L_{sd} - L_{sq})i_{sd}i_{sq}) \tag{2.23}$$

From the torque equations it can be seen that both the magnetic- and reluctance torque is dependent of the q-current, but only the reluctance torque is dependent on the d-current. To maximise the output torque per ampere the combination of the i_{sd} and i_{sq} should be optimised. First the identification of i_{sd} and i_{sq} is done by

$$
\begin{aligned}
i_{sd} &= I_{mag} \ \cos(\beta) \\
i_{sq} &= I_{mag} \ \sin(\beta)
\end{aligned}
\tag{2.24}
$$

Equation (2.24) is then inserted in (2.21) and results in

$$T_e = \frac{3n_p}{2}\left(\Psi_m I_{mag}\sin(\beta) + (L_{sd} + L_{sq})I_{mag}^2\sin(\beta)\cos(\beta)\right) \tag{2.25}$$

Since the maximum Torque per ampere is of interest the derivative of (2.25) is taken and set equal to zero

$$\frac{\mathrm{d}T_e}{\mathrm{d}\beta} = \frac{3n_p}{2}\left(\Psi_m I_{mag}\cos(\beta) + (L_{sd} - L_{sq})I_{mag}^2\cos(2\beta)\right) = 0 \tag{2.26}$$

There after the $\cos(\beta)$ is solved for, this gives

$$\cos(\beta) = -\frac{\Psi_m}{4(L_{sd} - L_{sq})I_{mag}} - \sqrt{\frac{1}{2} + \left(\frac{\Psi_m}{4(L_{sd} - L_{sq})I_{mag}}\right)^2} \tag{2.27}$$

A visualised example of the dq-current angle can be seen in Figure 2.2 where $L_{sd} < L_{sq}$, which is indicated by the negative d-current.

5

2.2   Machine topology background

The transverse flux machine topology is based on, as the name suggests, that the torque driven flux is flowing transversely inside the active machine. This means that the magnetic flux inside the active machine is moving in a 3D room instead of a 2D plane. In the transverse flux machine the soft magnetic steel can be used to wrap around the winding, as can be seen in Figure 2.3. In comparison from an conventional synchronous winded machine where the winding is wrapped around the soft magnetic steel [4], as shown in Figure 2.4. Both figures shows a simplified rotor with two magnetic polarities, the soft magnetic steel is shown in an dark oxidised color and the copper winding are shown as a polished copper colored surface.

A subcategory of transverse flux machine is the claw pole machine, where the poles are shaped as claws and wrapping around the magnetization source. Either the rotor, stator or both the rotor and stator can have this claw pole design. A claw pole rotor is shown in Figure 2.5 and a claw pole stator is shown in Figure 2.6.

Another aspect that should be explained is poly-phase structure. The poly-phase machines is a number of one-phase machines stacked on each other in the axial direction, forming an multi-phase machine. Each one-phase part is referred to as a stack and to create the electrical phase shift either the stator stacks or the rotor stacks are mechanically shifted. In this thesis a 3 phase, three stack poly-phase claw pole machine with the stator mechanically shifted 120-degrees is designed.
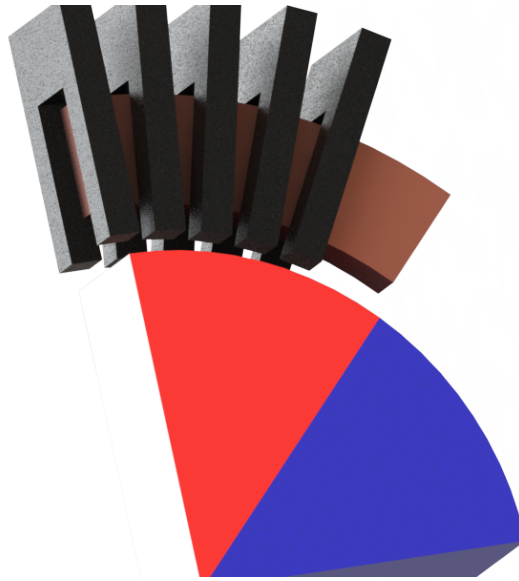
Figure 2.3: *An example of an transversal flux machine*
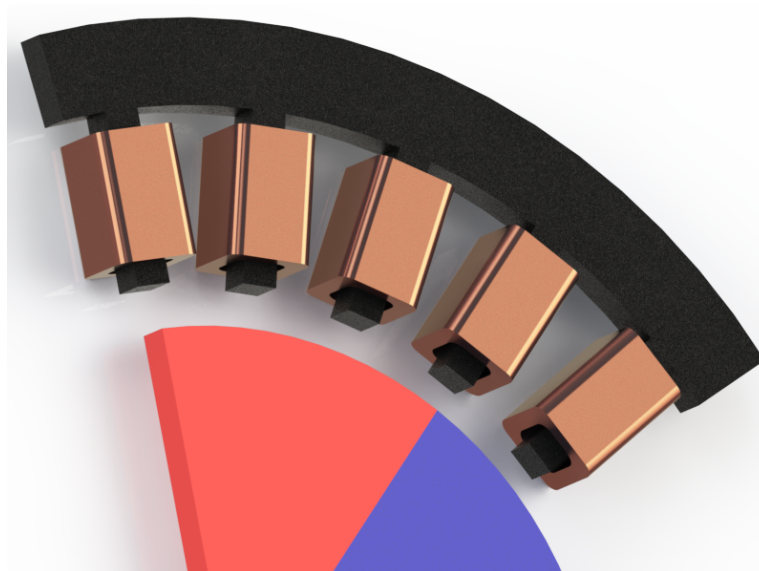

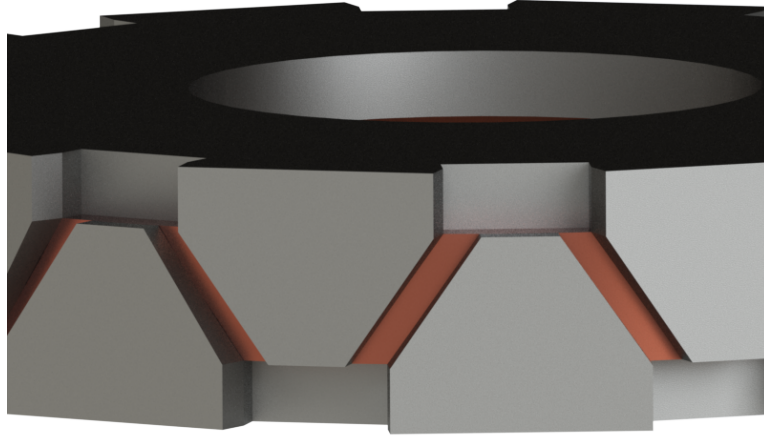Figure 2.4: *An example of a conventional radial flux machine*
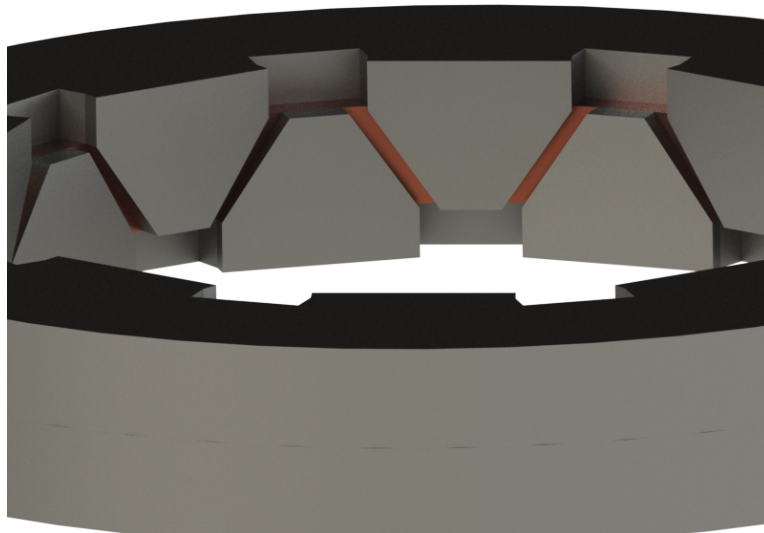
Figure 2.5: *An example of an claw pole rotor*

Figure 2.6: *An example of an claw pole stator*

2.3 Building aspects

The most common way of constructing an electrical 2D flux machine is by stacking laminated sheets of electrical graded steel, this is done to decrease losses from eddy currents. There are three main techniques that are used to cut out the geometry, stamping, water-jet cutting and laser cutting. Stamping is used in mass production since the price per laminate is low but the design cost for stamping tools is high. Laser or water-jet cutting is mainly used for prototyping or small-scale production since the cutting speed is relatively slow and costly in comparison to stamping [6].

When the flux geometry changes from 2D to 3D the laminated sheet method may not be adequate to lowering the eddy currents. For 3D flux applications soft magnetic composite materials is often used. For mass production soft magnetic composite material parts is usually sintered into shape. But for prototyping or small series, the sintering method becomes expensive because of high tooling costs. For this reason companies like Höganäs have developed specialised soft magnetic prototyping materials, which makes drilling, turning and milling possible, see apendix for datasheet. Even if the machinability of the soft magnetic prototyping material is better than the conventional soft magnetic materials, there are some things that needs to be considered. When milling, the tooling needs to be very sharp preferably new and unused carbide tools for aluminium or plastic. The material should always be supported, preferably climb milling used and cutting out of edges should be avoided. A common problem when machining soft magnetic materials is chapping, where edges is chipped and resulting in uneven edges.

2.4 Theory used in FE-calculations

In this subsection the basic behind the magnetic relations, later used to design and verifying the electrical machine, will be defined.

2.4.1 Reluctance torque

Assume that a coil is wounded around a ferromagnetic toroid with N number of turns and the current I. This can be connected to the magnetic field intensity by Ampère's circuital law as

$$\oint_c \bar{H} \cdot \mathrm{d}l = NI \tag{2.28}$$

If the ferromagnetic toroid have a small air gap the magnetic field intensity differs in the air gap from the ferromagnetic material. The magnetic field intensity can be rewritten to magnetic flux density using the constitutive equation

$$H = \frac{B}{\mu} \tag{2.29}$$

This is then set into (2.28) and integrated over the toroid with the mean radius r which results

in

$$\frac{B}{\mu_{fe}}(2\pi r - l_g) + \frac{B}{\mu_0}l_g = NI \tag{2.30}$$

After modification the result is

$$B = \frac{\mu_0\mu NI}{\mu_0(2\pi r - l_g) + \mu l_g} \tag{2.31}$$

since the magnetic flux density is constant in the geometry the magnetic flux can be calculated using

$$\Phi = \int_s B \cdot \mathrm{d}s = BS \tag{2.32}$$

Where S is the cross section area of the toroid. Equation 2.32 is then combined with (2.31) and results in

$$\Phi = \frac{NI}{\frac{(2\pi r - l_g)}{\mu S} + \frac{l_g}{\mu_0 S}} \tag{2.33}$$

This can then be rewritten as

$$\Phi = \frac{NI}{\Re_{fe} + \Re_g} \tag{2.34}$$

Were

$$\Re_{fe} = \frac{2\pi r - l_g}{\mu S} = \frac{l_f}{\mu S}$$
$$\Re_g = \frac{l_g}{\mu_0 S} \tag{2.35}$$

is the reluctance equations for the ferromagnetic geometry and the air gap. The inductance can then be calculated using

$$L = \frac{N\Phi}{I} = \frac{N^2}{\Re_{fe} + \Re_g} \tag{2.36}$$

The force applied on the rotor equals to

$$F = \Delta W_m = \Delta\frac{Li^2}{2} \tag{2.37}$$

Equation (2.36) is then inserted in (2.37) to give the force dependent on the reluctance as

$$F = \frac{i^2 N^2}{2\Delta(\Re_{fe} + \Re_g)} \tag{2.38}$$

The total reluctance torque can then be approximated using

$$T_r \approx n_P F r \tag{2.39}$$

where n_P is the number of pole pairs, F the force and r rotor radius.

2.4.2 Magnetic torque

Since the magnetic path can be expressed as a magnetic circuit with two air gaps and two reluctance paths as seen in Figure 2.7. With the approximation of the magnetic flux generated from the permanent magnet to be constant, the total flux can be calculated as

$$\Phi_{tot} = \Phi + \Phi_m \tag{2.40}$$

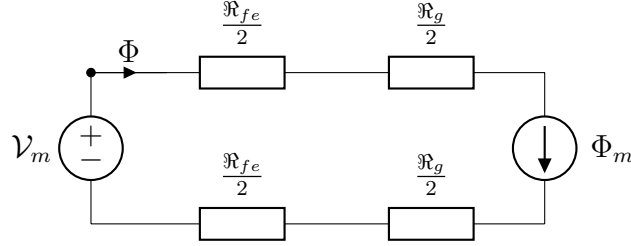were Φ_m is the magnetic flux generated from the permanent magnet.

Figure 2.7: *Magnetic circuit model. $\mathcal{V}_m$ is the mmk and Φ_m the permanent magnet flux.*

The magnetic work created with the permanent magnet flux can then be calculated as

$$W_m = \frac{i\Phi_m}{2} \tag{2.41}$$

The magnetic force is then calculated using

$$F = \nabla W_m \tag{2.42}$$

and the torque can then be calculated using

$$T = -\frac{\partial W_m}{\partial \theta} \tag{2.43}$$

3 Design

In this section the design specifications and limitations for the machine, will be derived and explained. After that, the optimisation of the electromagnetic circuit is done. This is mainly done by changing the geometry of the magnetic path, the size of the magnet and the number of turns in the coil.

The limitations is mostly set by the delivered geometry of the soft magnetic material. The material used is Somaloy prototyping material, the datasheet is included in the Appendix. The Somaloy prototyping material is delivered as cylinders with a height of 20 mm and a diameter of 120 mm, which sets the geometrical limitations of the stator and rotor parts. The stack height will therefore be set to be 20 mm and the stator outer diameter will be set to 120 mm.

The design process starts with analytical calculations, so that the setup for the FE calculations can be verified. When the first verification is done, it is time to add the magnet to the machine. This is done by first calculating the size of the magnet, then adding the magnet into the FE calculations for detailed studies. When the FE calculations have been verified against the analytical calculations, then it is time to start to optimise by changing geometry and parameters. To be able to know what to change, the magnetic flux density plots are being used, the high spots are being treated to lower the magnetic flux density and the material at low spots are being removed to lower the weight of the machine and leakage inductance. The number of turns in the winding is used to control the magnetic flux. When the electromagnetic design is in a finished state, it is time to add the mechanical features needed to be able to assemble the machine. Finally a basic thermal simulation is done to find thermal limitations.

3.1 Verification

The inductance and resistance is chosen as the verification parameters, so for the verification, the inductance and resistance need to be calculated. Since the relation between inductance and reluctance is defined, in (2.36), the reluctance should be calculated. To be able to calculate the reluctance, the magnetic flux path needs to be defined. Therefore some initial values need to be defined. As the initial values, the rotor diameter was set to half of the stator outer diameter, this results in a rotor diameter of 60 mm. The number of pole pairs was set to $N_p = 4$, this was done since it seemed reasonable as an initial value. The air gap length was set to be 0.5 mm and the width of the teeth at the air gap was set to be the same width as the non aligned area calculated as

$$teeth\ width = \frac{360°}{4N_p} = 22.5° \tag{3.1}$$

which will translate to mm by

$$s = \frac{22.5°}{180°}\pi r \approx 11.8\ mm \tag{3.2}$$

where r is the radius of the rotor. The verification geometry is shown in Figure 3.1. The arc length is then multiplied with the stack height to get the cross-section area of the air gap. The cross-section area is then derived to
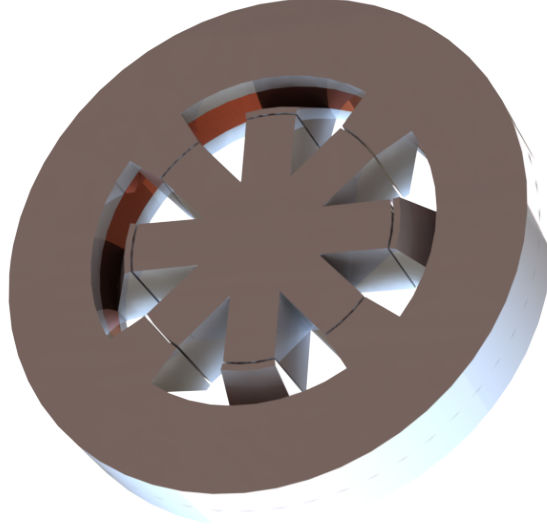
Figure 3.1: *Rendering of the first iteration*

$$a = sh = 236 \ mm^2 \tag{3.3}$$

The reluctance in the air gap can then be calculated using (2.35). The reluctance per air gap then becomes

$$\Re_g = \frac{l_g}{a\mu_0} = \frac{0.5 \times 10^{-3}}{4\pi \times 10^{-7} \times 236 \times 10^{-6}} \approx 1.7 \times 10^6 \tag{3.4}$$

The total reluctance depends on the pole pairs and is calculated as

$$\Re_{g \ tot} = \frac{\Re_g}{N_p} = \frac{1.7 \times 10^6}{4} = 425 \times 10^3 \tag{3.5}$$

The inductance contributed from the air gaps, is calculated as

$$L_g = \frac{N^2}{2\Re_{g \ tot}} = \frac{10^2}{2 \times 425 \times 10^3} = 117.7 \ \mu H \tag{3.6}$$

From the first FE calculation it could be seen that there was leakage inductance interfering with the calculated inductance. The energy density plot of the FE calculation can be seen in Figure 3.2. It can be seen that there is magnetic energy behind the stator teeth and on the outside of the air gap, which indicates that the fringing effects in this areas need to be considered.

First the inductance from the air gap needed to be calculated. This was done by setting the relative permeability to 4×10^6 in the ferromagnetic material. The relative permeability of the copper windings and all air except in the air gap was set to 0.02, in order to decrease the influence of this regions. This gave a FE calculated inductance, $L = 117.4 \ \mu H$ which can be compared to the calculated inductance of 117.7 μH, for the air gap.
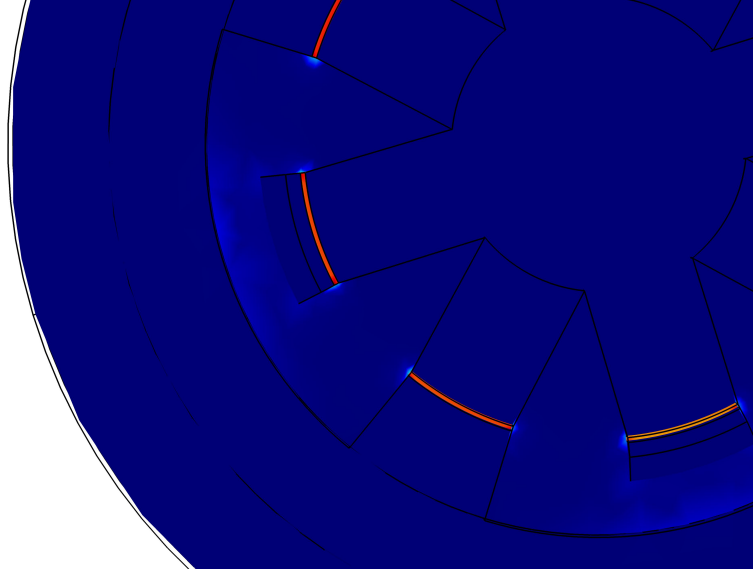
Figure 3.2: *Energy density distribution in the verification simulation, with default permeability*

The inductance in the air gap with fringing was calculated from reluctance using

$$\Re = \frac{1}{\mu_0 \left(\frac{s}{l_g} + \frac{2}{\pi}(1 + \ln \frac{\pi h}{2l_g}) \right)} = 30.619 \times 10^3 \ m/H \tag{3.7}$$

which is a fitted version of (17) in [7], were h is the height of the expected fringing. From that equation the reluctance meter is calculated, the reluctance is calculated by dividing with the stack height h = 20 mm. The expected fringing height was set to 5 mm, which is 10 times the air gap height. The calculated inductance with fringing was 130.6 μH.

FE-calculation of the fringing was done by adding a separating region behind the stator teeth with a relative permeability of 0.02. The relative permeability of the copper winding were set to 0.02, while the relative permeability for the air domains was set to 1. The resulted FE calculated inductance was 130.3 μH.

In Figure 3.2 it could be seen that it was energy distribution behind the stator teeth, which indicates leakage inductance. This leakage inductance was calculated using

$$\Re = \frac{1}{\mu_0 \left(\frac{s}{l_{back}} + \frac{4}{\pi}(1 + \ln \frac{\pi h_{bst}}{4l_{back}}) \right)} = 431.96 \times 10^3 \ m/H \tag{3.8}$$

which is a fitted version of (16) in [7], where $l_{back} = 8 \ mm$ is the distance between the stator teeth backside and the other stator parts, $h_{bst} = 5 \ mm$ is the height of the stator stack behind the stator teeth. The resulting calculated inductance for this back side leakage inductance is 37.0 μH. The sum of the inductances becomes 167.7 μH. The FE calculated inductance without any domain constrains except for the copper windings, which had a relative permeability of 0.02, was 167.3 μH.

The leakage inductance contribution from the copper winding was calculated using a fitted version of (15) in [7]. This resulted in a reluctance of

$$\Re = \frac{1}{\mu_0 \left(\frac{w_{winding}}{2h_{winding}} + \frac{1}{\pi}(1 + \ln \frac{\pi h_{bst}}{2h_{winding}}) \right)} = 1.0733 \times 10^6 \ m/H \tag{3.9}$$

were $w_{winding} = 10 \ mm$ is the width of the winding, $h_{winding} = 10 \ mm$ is the height of the winding and $h_{bst} = 5 \ mm$ is the height of the stator stack behind the stator teeth. Since this is in m/H the result was then divided with the interfering length which was calculated as

$$l_{coil \ fringing} = \mathcal{O}_{bst} - 2N_p l_{teeth \ bst} = 125.7 \ mm \tag{3.10}$$

were $\mathcal{O}_{bst} = 251.3 \ mm$ is the circumference behind the stator teeth, $l_{teeth \ bst}$ is the arc length of the teeth in the connection at the teeth and the stator base. The resulting leakage inductance at the coil is 11.7 μH, which gives an total summed inductance of 179.4 μH. The FE calculated inductance with defaulted domain and regions was 182.9 μH

With the fringing effects, defaulted domains and relative permeability and the relative permeability of the ferromagnetic material was changed to 400, which is close to the maximum relative permeability of the Material used. The calculated inductance become 140.8 μH and the FE calculated inductance become 138 μH.

The winding resistance can be calculated using the resistivity of copper $\rho = 1.68 \times 10^{-8}$, the cross section area of the winding wire $a_{wire} = 6.4 \ mm^2$, the length of one winding turn $l_{windingturn} = 0.28 \ m$ and the number of turns $N = 10$. The winding resistance then becomes

$$R = N \times \rho \frac{l_{winding}}{a_{wire}} = 7.4 \ m\Omega \tag{3.11}$$

The FE calculated winding resistance was 7.4 $m\Omega$, using the built in global evaluation for the coil resistance in Comsol Multiphysics, which is equal to the calculated one.

3.2   Adding a magnet

The magnet needs to be added to the model to be able to verify the FE model against analytical calculations. The dimensions of the magnet is not important at this stage of the design, since the dimensions of the magnet will be changed in the iterative refinement process.

The height of the magnet is set to be 6 mm, and it will be buried 2 mm on each side to lower the magnetic flux density in the corners. Since there is going to be an axle through the magnet and the magnet needs to be magnetised in the axial direction, the magnet needs to have the shape of a cylinder with a center hole. Also the axle needs to be made of a nonmagnetic material like nonmagnetic stainless steel, with a relative permeability approximated to air. The radius of the axle is set to be 6 mm, since this is sufficient for the torque loads. For the verification the inner radius of the magnet is set to be 6 mm, the same as the radius of the axle. The outer radius is set to be 9 mm, half of the height of the magnet added on the inner radius.

3.3   Torque calculation

To be able to verify the FE calculations an analytical calculation on a torque step around aligned position was done. The torque was calculated using (2.43) were $W_m = \frac{LI^2}{2}$ and I was set to 50 A. This then becomes

$$T = -\frac{\partial L}{\partial \theta}\frac{I^2}{2} \tag{3.12}$$

Which is only valid in the simplified linear case with linear Media, which is used for this verification. The variation of inductance at different angles was then calculated around the aligned position, with a step of 0.1 degrees. The change in inductance was calculated from the change of the air gap cross section area depending on the angle. The inductance with fringing was then calculated using the same method as for the verification of the inductance, where the space for the magnet was added as a air gap of 2 mm since the other parts of the magnet was buried 2 mm in the rotor parts and the magnet was 6 mm high. The width of the magnet was 3 mm as calculated. Reluctance with fringing effect at the magnet was calculated using

$$\Re = \frac{1}{\mu_0 \left(\frac{w_{magnet}}{2h_{magnet\ gap}} + \frac{1}{\pi}\left(1 + \ln \frac{\pi h_{buried}}{2h_{magnet}}\right)\right)} = 0.92279 \times 10^6\ m/H \tag{3.13}$$

which is a fitted version of (17) in [7]. Since this gives the unit $m/\Re$, the result was then divided with the outer circumference of the magnet, which was 56.6 mm. The inductance at different angles was calculated and inserted into (3.12).

The analytical torque was constant, within the accuracy, around ± 1 degree and equal to 0.098 Nm. The plot of the analytical torque can be seen in Figure 3.3, when the fringing effect was considered. Which can be compared to the FE calculated torque, which was 0.098 Nm around ± 1 degree.
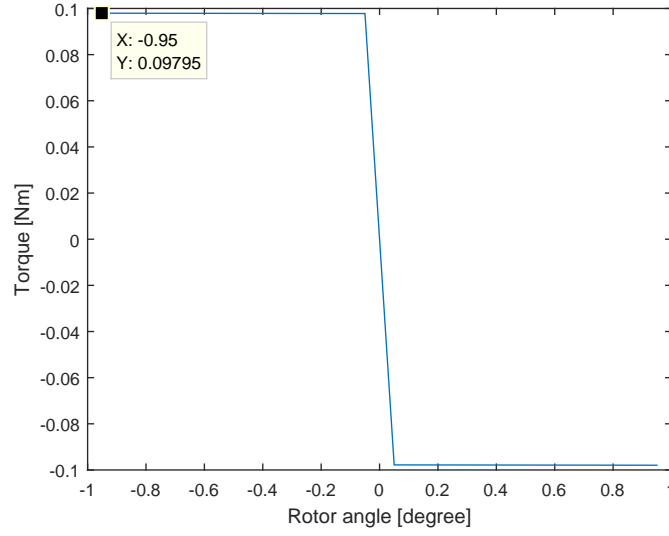
Figure 3.3: *The analytical torque at ±1 degree around aligned position*

3.4 Back-EMF calculation

The analytical calculations of the Back-EMF was calculated using

$$emf = \omega_m \frac{\partial \Psi}{\partial \alpha} \tag{3.14}$$

where ω_m is the mechanical angular frequency of the rotor and $\alpha = \omega_m t$. Ψ is calculated as in (2.32) where B is the remanent flux density of the magnet and S the cross section area of the air gap. The cross section area was changed in the same way as for the torque calculations. The resulting back-EMF at 1 Hz was calculated to -4.2 mV at aligned position. Which can be compared with the FE calculated back-EMF which were -4.1 mV at aligned position, shown at 0 degree in Figure 3.4.
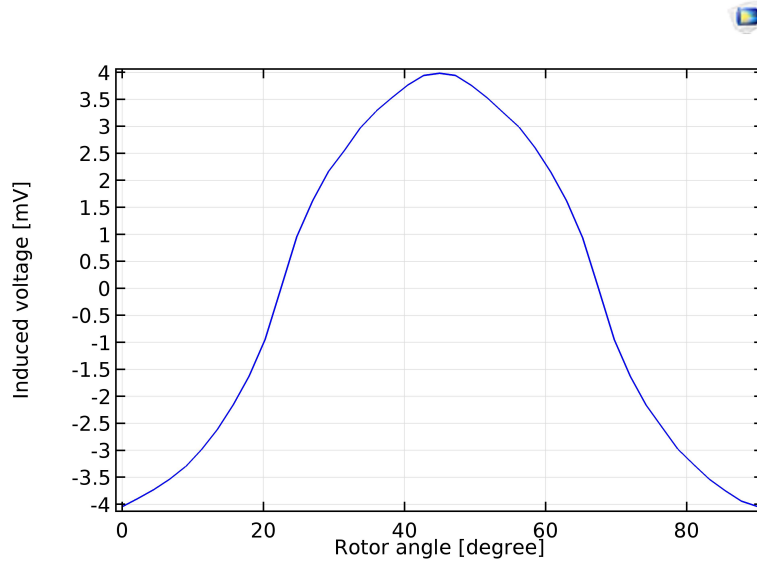
Figure 3.4: *The FE calculated back-EMF at 1 Hz with open coil terminals*

3.5 Final geometry

Under several iterations, the geometry was changed to even out and lower spikes in the magnetic flux density distribution. Fillets were added and changed to smother corners. The magnet size changed to an inner diameter of 25 mm, an outer diameter of 32.4 mm and a height of 6 mm. The magnet was buried 2 mm on each side in the rotor to lower magnetic flux density in the corners. The magnets precise measurements was set by what was available at the manufacturer at that moment. The number of turns in the coil was changed to 13 turns and the crosssection area of the wire was changed to 1.1 mm^2. The final mechanical geometry can be seen in section 3.6.

The phase resistance was FE-calculated to 62.5 mΩ. The inductance varies with rotor position in a way that is shown in Figure 3.5. The average self-inductance was FE-calculated to 207.5 µH, and the varying inductance was FE-calculated to 97.5 µH. Since the FE-calculations have been done in only one phase the mutual inductance was approximated to 0. The back-emf was FE-calculated to 0.0206 V/Hz. This parameters were then transformed over to the dq-domain using the method explained in 2.1 and can be seen in Table 3.1.

Table 3.1: FE-calculated parameters in the dq-domain

R_s	62.5 mΩ
L_{sd}	354 µH
L_{sq}	61 µH
Ψ_m	0.0206 V/Hz

Since the equivalent circuit parameters is calculated, the dq-voltages and dq-currents can then be calculated using (2.19), by setting a maximum absolute voltage to 48 V and the current angle equal to the MTPA angle shown in Figure 3.6.
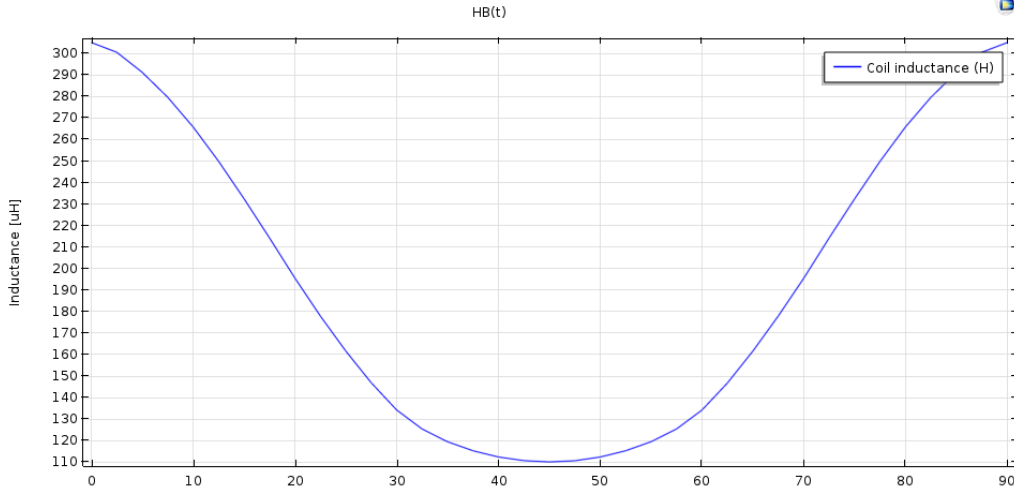
Figure 3.5: *FE calculated inductance curve for final geometry depending on mechanical rotor angle*
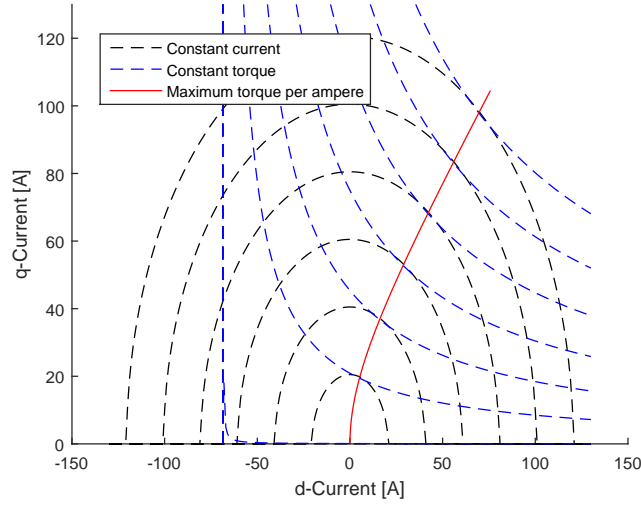
Figure 3.6: *The voltage components speed characteristics for MTPA calculated from FE-calculated values*

3.5.1 Nominal torque

For the nominal torque the nominal current is 20 A and the current speed characteristics can be seen in Figure 3.7, where the dq-components contributions is calculated from the MTPA angle. Figure 3.8 shows the voltage speed characteristics with the dq-component contribution. The absolute voltage and current speed characteristics is shown in Figure 3.9

The nominal torque is then calculated using (2.21), the magnetic torque contribution is calculated using (2.22) and the reluctance torque contribution is calculated using (2.23). This torque contributions is then plotted against mechanical speed and is shown in Figure 3.10. The maximum nominal output power at different speeds is shown in Figure 3.11.

19
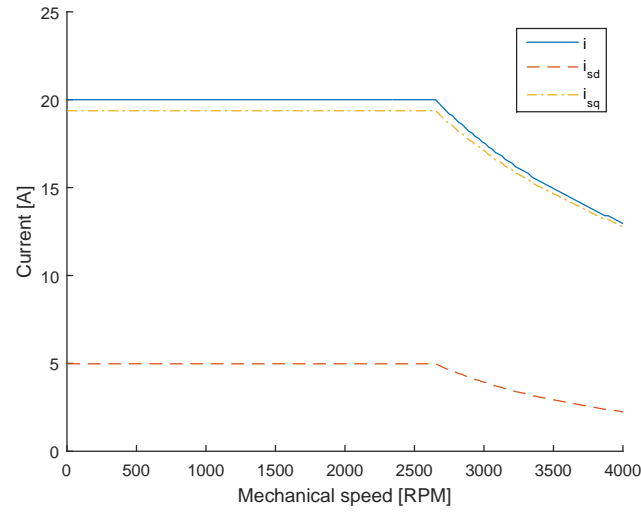
Figure 3.7: *Maximum current components speed characteristics for nominal torque*
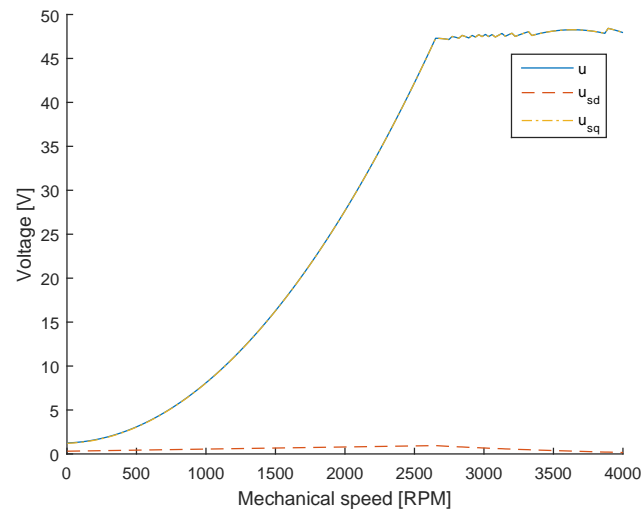
Figure 3.8: *The voltage components speed characteristics for nominal torque*
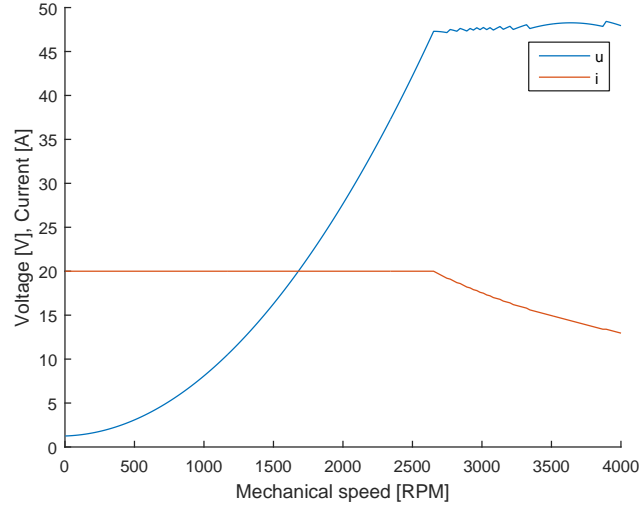
Figure 3.9: *Voltage and current per speed characteristics for nominal torque calculated from FE-calculated values*
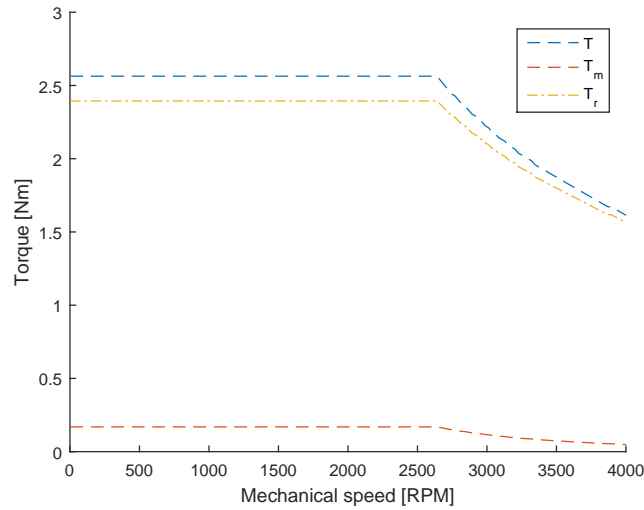
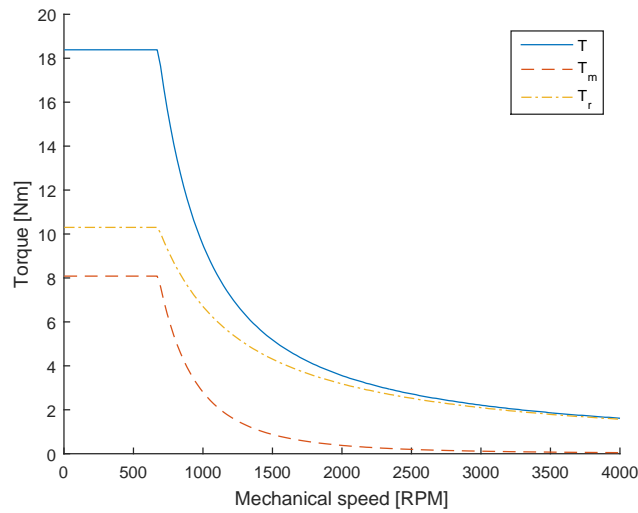Figure 3.10: *Maximum nominal torque components at different speed calculated from FE-calculated values*

21
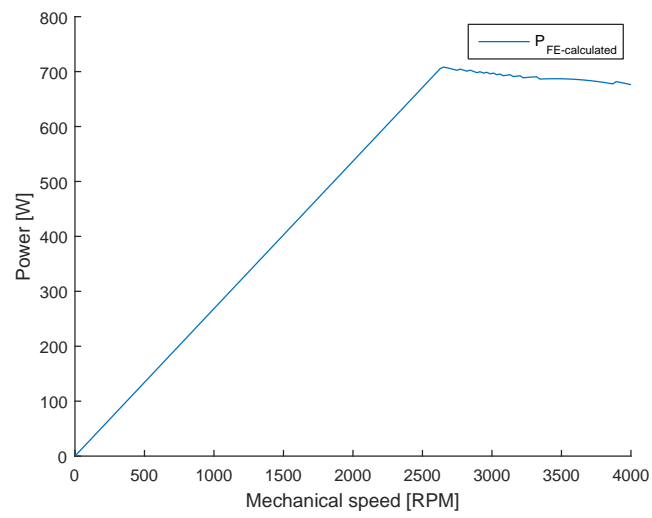
Figure 3.11: *Maximum nominal power at different speed calculated from FE-calculated values*

3.5.2 Peak torque

For the peak torque the current is 100 A and the current speed characteristics can be seen in Figure 3.13, where the dq-components contributions is calculated from the MTPA angle in Figure 3.6. Figure 3.12 shows the voltage speed characteristics with the dq-component contribution. The absolute voltage and current speed characteristics is shown in Figure 3.14
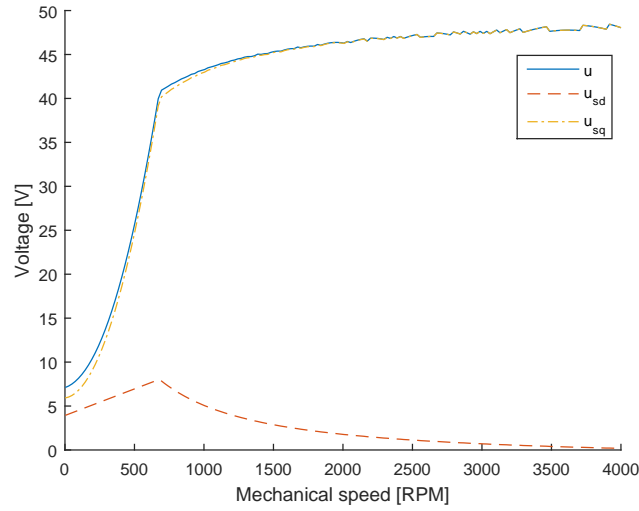
Figure 3.12: *The voltage components speed characteristics for MTPA calculated from FE-calculated values*
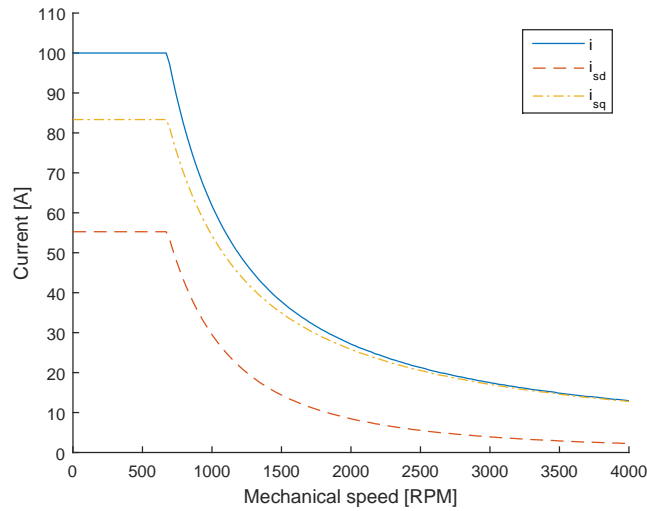
Figure 3.13: *Maximum current components speed characteristics for MTPA from FE-calculated values*
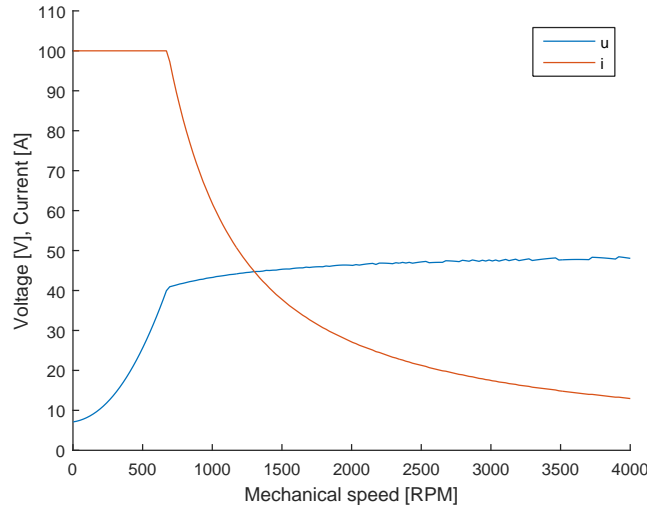
Figure 3.14: *Voltage and current per speed characteristics calculated from FE-calculated values*

The peak torque is calculated in the same way as for the nominal torque case. This torque contributions is plotted against mechanical speed and is shown in Figure 3.15. The maximum output power at different speeds is shown in Figure 3.16.

Figure 3.15: *Maximum torque components at different speed calculated from FE-calculated values*
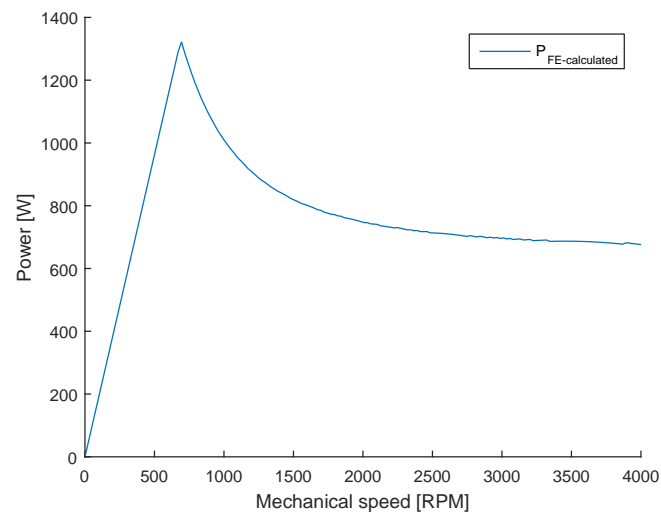
Figure 3.16: *Maximum power components at different speed calculated from FE-calculated values*

3.6 Mechanical

The geometry is developed to utilise the possibility to stack a common design on top of each other to create the final geometry. One rotor segment can be seen in Figure 3.17. The permanent magnet has a pocket to be lowered into, this gives the magnet more mechanical stability and lower the magnetic stress in corners. The mechanical fastening between the rotor and the axle is done by using a key and keyway. Since the middle segment is turned upside down a design of the rotor part with the keyway angular shifted is needed. This makes the keyway solution non fit for mass production since it duplicate the needs of tooling to sinter the rotor. For prototyping purposes the keyway solution works fine, since the milling method is used.
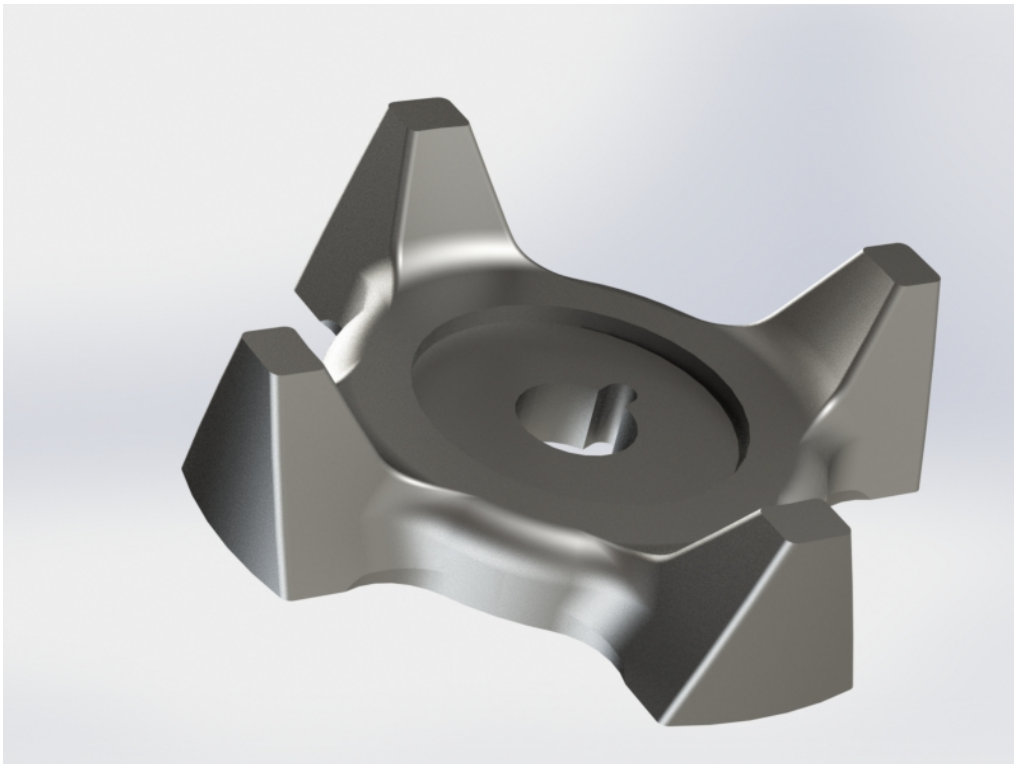
Figure 3.17: *Rendering of a rotor segment*

The stator is mechanically held together with six threaded rods placed evenly through the outer rim, the mounting holes can be seen on a single stator part in Figure 3.18. This fastening also facilitates for an easy phase shift between each phase, since the stator needs to be mechanically shifted 120 electrical degrees which transfers to 60 mechanical degrees.

The 1 phase machine is then assembled as the exploded view shown in Figure 3.19. Where the winding is represented as a solid copper ring and the magnet can be seen as the shiny stubby cylinder. The active machine assembly can be seen in Figure 3.20. In the stator the 120 electrical degrees phase shift can be visualised by looking at the stator teeth. At the rotor it can be seen that the middle segment is turned upside down, this is done to utilise the magnetic field so that each linked teeth have the same magnetic polarisation.
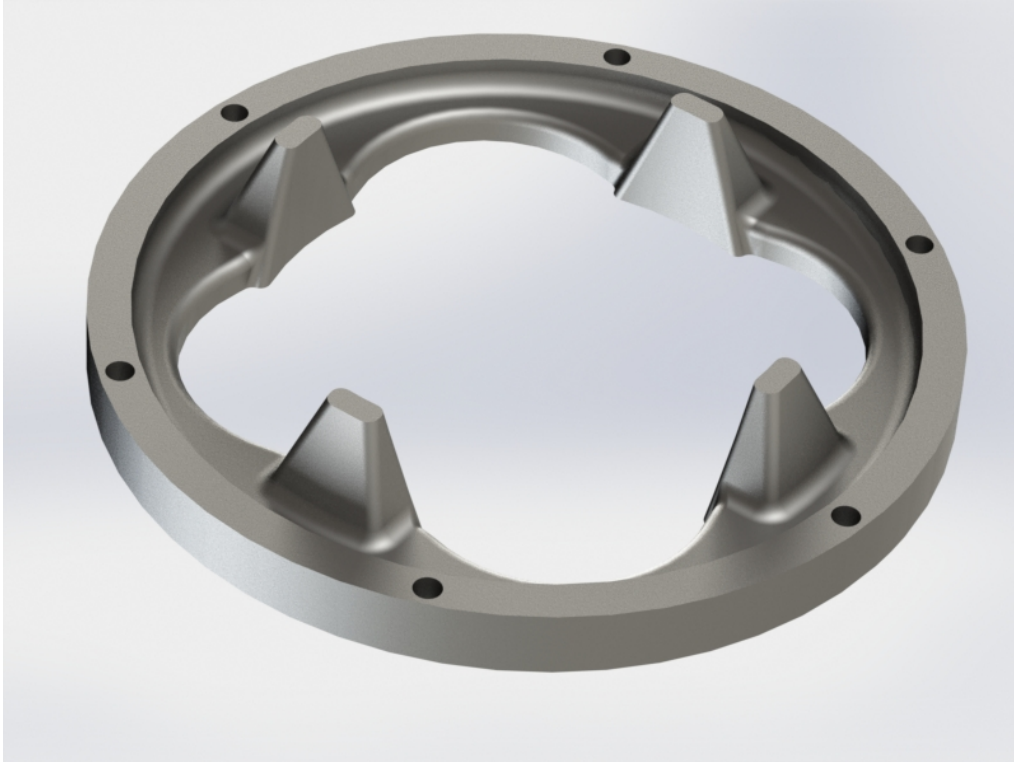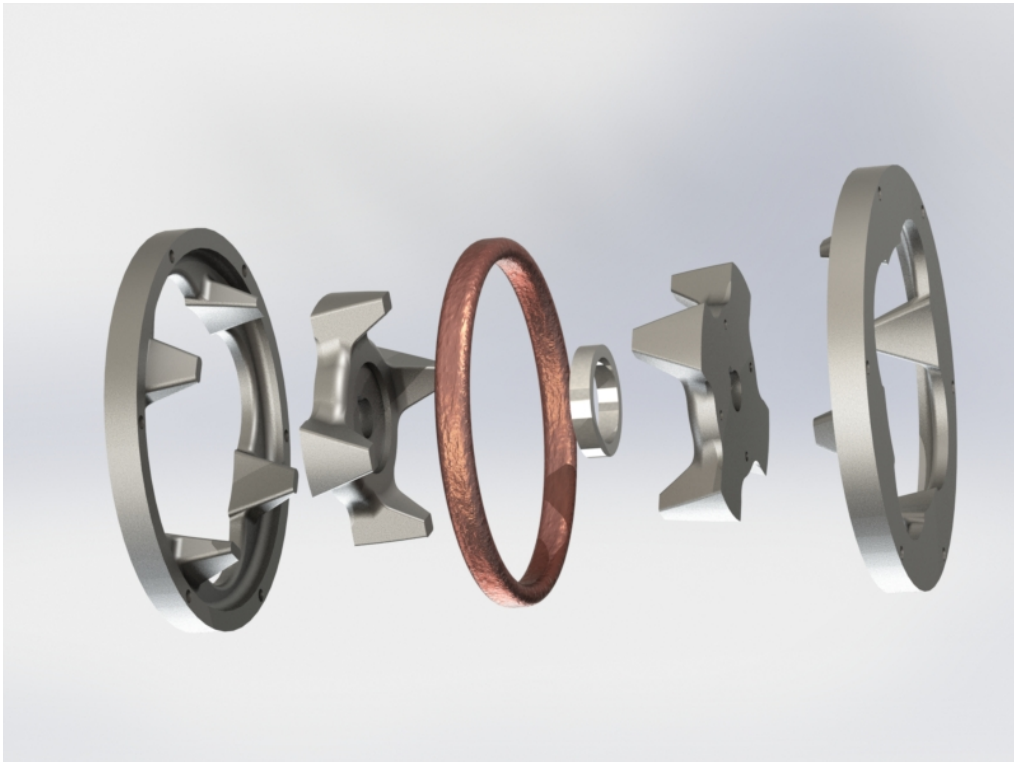
Figure 3.18: *Rendering of a stator segment*

Figure 3.19: *Exploded view of 1 phase from left to right: stator segment, rotor segment, copper windings, permanent magnet, rotor segment and stator segment.*
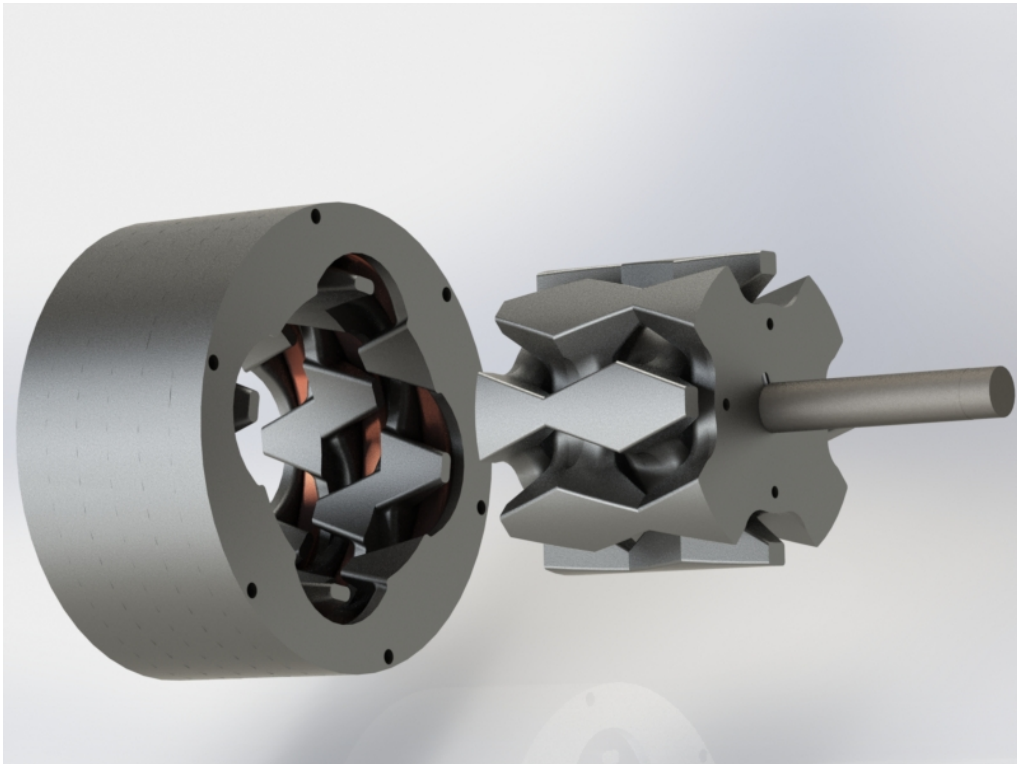
27

Figure 3.20: *Visualisation of the active 3 phase machine*

3.7 Thermal

To keep the machine from braking from thermal stress, a simple thermal simulation have been done. Where both the nominal load case and maximum torque case have been under consideration. Cooling fins have been designed to keep the nominal load temperature under 150°C, since this is highest temperature the Somaloy prototyping material is guaranteed to withstand without changing electromagnetic properties. A CAD drawing of the cooing fins can be seen in Figure 3.21.
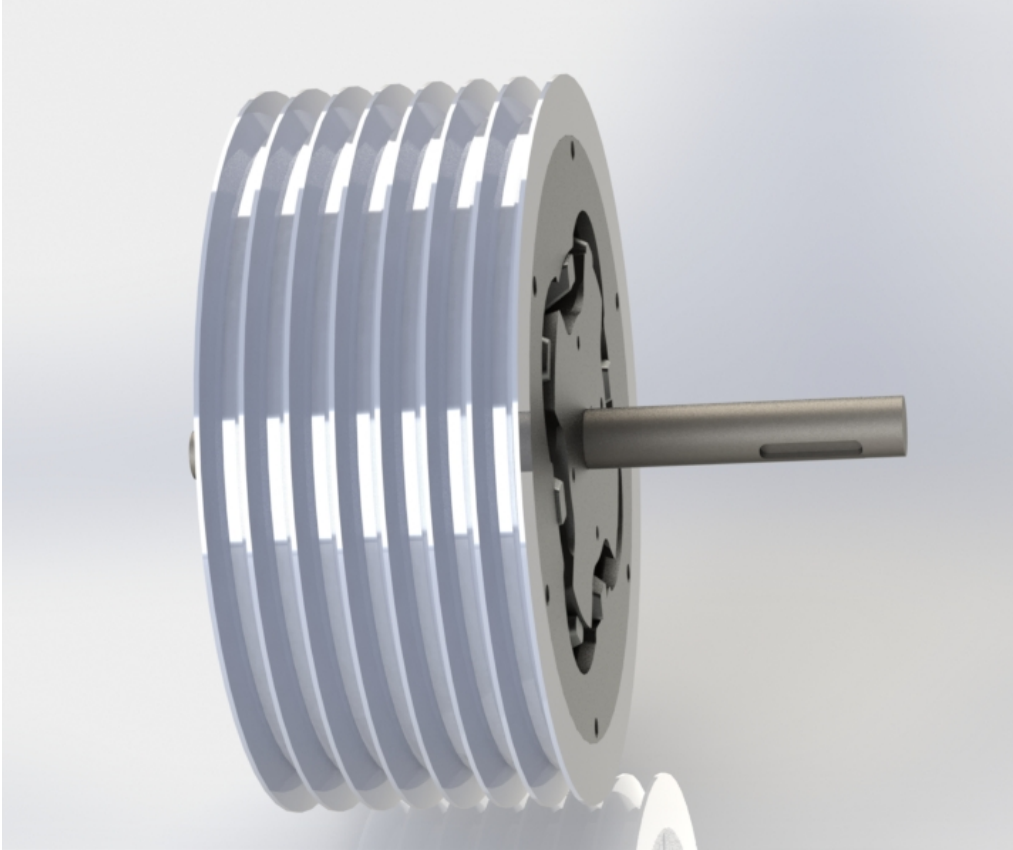
Figure 3.21: *Rendering of cooling fins added to the active machine*

For the time dependent simulation the copper losses was calculated by $P_{cu} = R \times I^2$ where I is equal to 20 A for the nominal case and 100 A for the peak torque case and $R = 62.5\ m\Omega$ in both cases. The heat rate was then distributed in each winding. The heat rate power for the iron losses was set to 42 W calculated from the datasheet, which can be seen in Appendix. Natural convection was used for heat dissipation. The FE-simulation results can be seen in Figure 3.22, it is clear that the windings is going to be the most sensitive and hardest to keep cool under operation. For this reason protective thermal switches are placed on the windings to protect the windings from over heating. The winding temperature over time for the nominal load case can be seen in Figure 3.23 and for peak torque load in Figure 3.24.
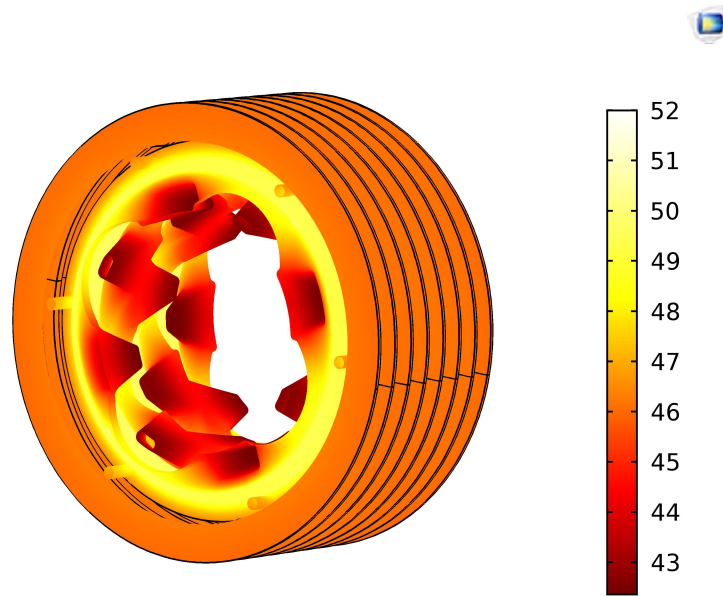
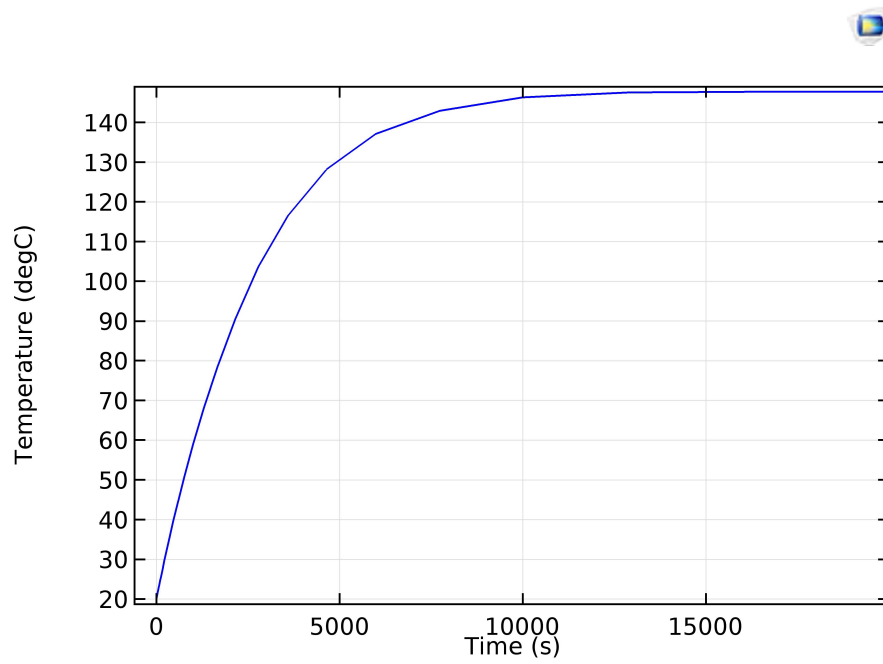Figure 3.22: *Visualisation of temperature inside the stator after 60 s*

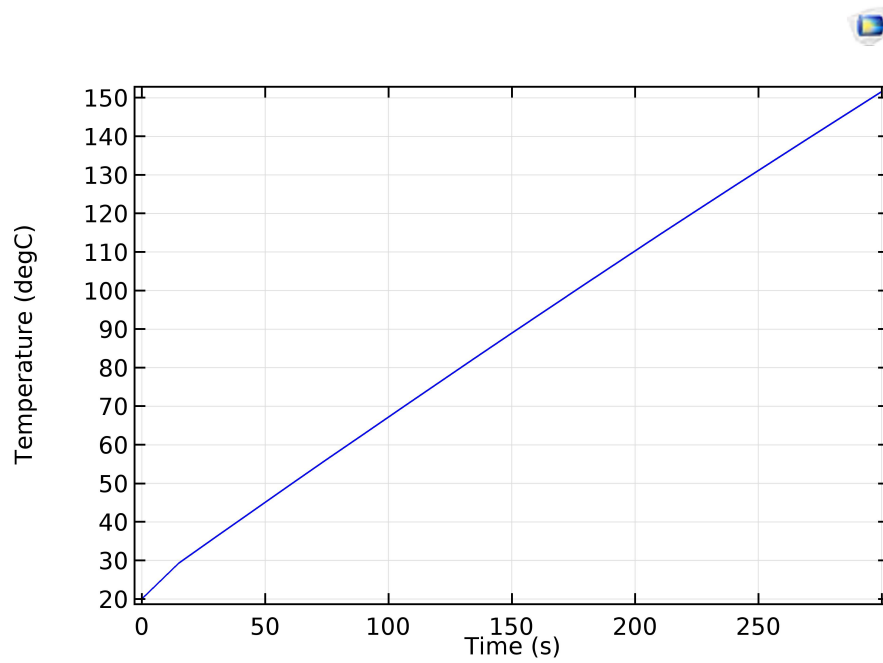Figure 3.23: *The winding temperature over time at nominal load*

Figure 3.24: *The winding temperature over time at peak torque*

4 Prototyping

The active machine and sides of the housing is machined using an 3-axis CNC mill. The material used for the active machine is Somaloy prototyping material. The datasheet can be seen in Appendix. Since the material is a sintered soft magnetic material, the machining of the material is relatively complex, because of chapping at edges.

4.1 Rotor

The fastening of the rotor was done using a jig, were the rotor was screwed down against the jig. The jig with a bolted rotor piece can be seen in Figure 4.1 and the threaded holes can be seen in Figure 4.2. The jig was also used to give the rotor some extra stability at the bottom, which was important to minimise the chapped edges. The resulting chapped edges can be seen in Figure 4.3. To minimise chapped edges sharp milling tools were needed, therefore milling tools for aluminium were used. A degradation of the milling tools were seen by a rapid increase of chapping. So the milling tools needed to be changed between every other part.
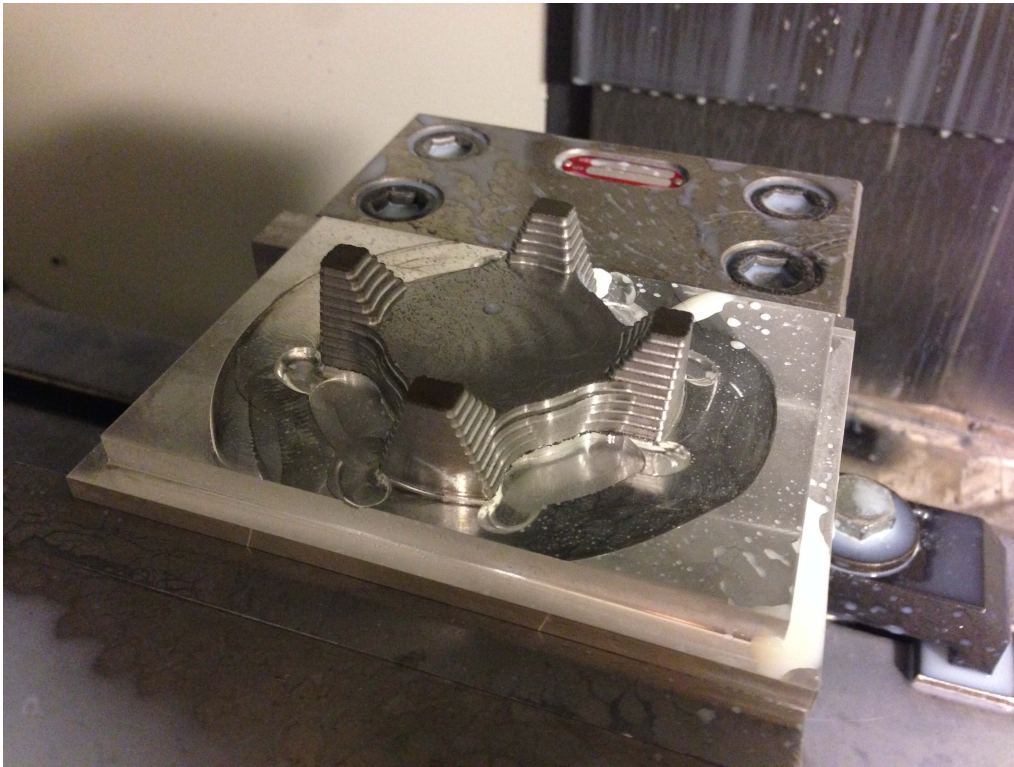
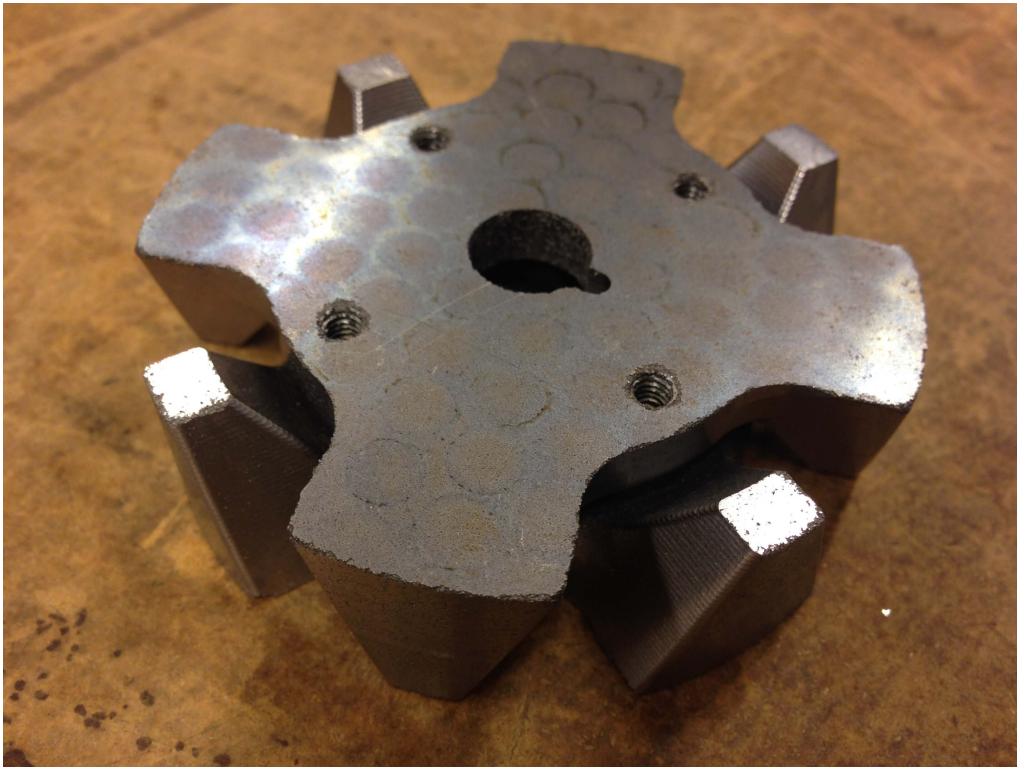Figure 4.1: *Rotor jig with an mounted rotor part in the mill*

Figure 4.2: *Rotor segments with jig mounting holes*

Figure 4.3: *Chapped edges on final rotor parts*

The rotor parts were then mounted as seen in Figure 4.4. The rotor segment and magnet in the middle segment is turned upside down to align the magnetic flow in the rotor.

Figure 4.4: *Final mounted rotor with axle and bearings*

4.2   Stator

The stator was milled in a similar way as the rotor, it was screwed down to a jig. The outer diameter and the outer sides of the teeth were milled first. After this the outer part was pressed down using clamps, so the inner part of the stator could be milled. The fastening after the milling of the outer part can be seen in Figure 4.5, and the mounting holes for the fasteners can be seen outside the outer diameter of the stator. The problem with chapped edges were the same for the stator and can be seen in Figure 4.6
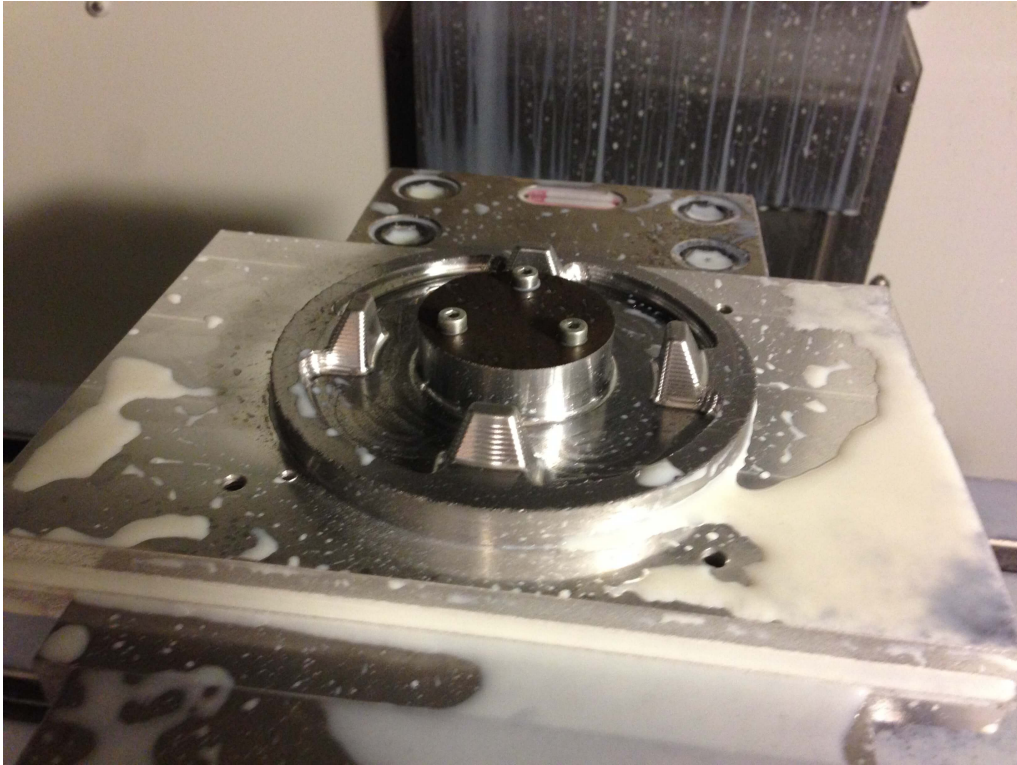
Figure 4.5: *Stator jig with an mounted stator part in the mill*

Figure 4.6: *Chapped edges on one of the final stator parts*

4.3 Assembly

To be able to hold it all together two end plates were milled and the final parts can be seen in Figure 4.7
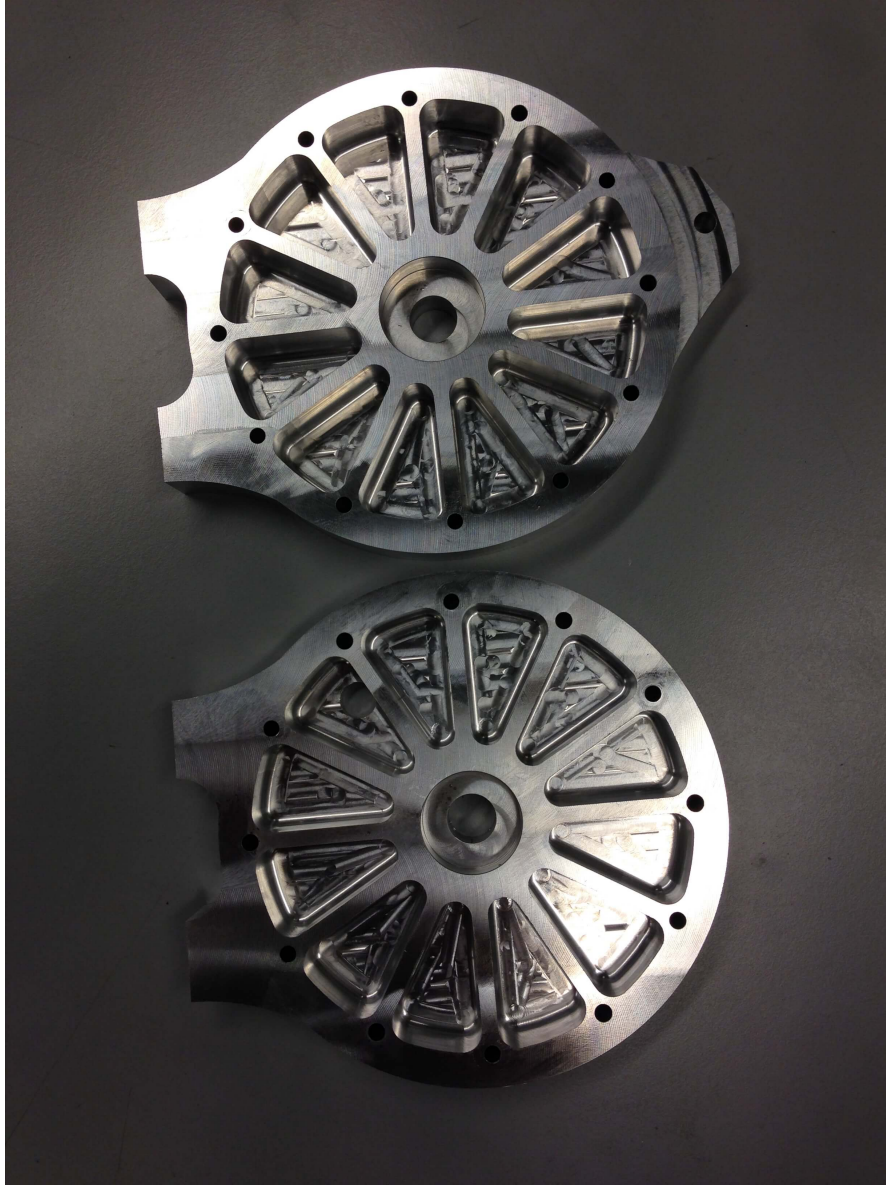

Figure 4.7: *The sides to hold the machine together with bearing mounts*

The windings for the machine were done by utilising a jig. A lathe was used to wind up the windings on the jig with the correct dimensions, to easily fit into the stator segments. The winding jig setup can be seen in Figure 4.8.

The cooling mantle was turned and can be seen in Figure 4.9 mounted together with the stator. The final assembly of the stator can be seen in Figure 4.10. Thermal switches and a temperature sensor have been mounted on the windings for protective purposes.
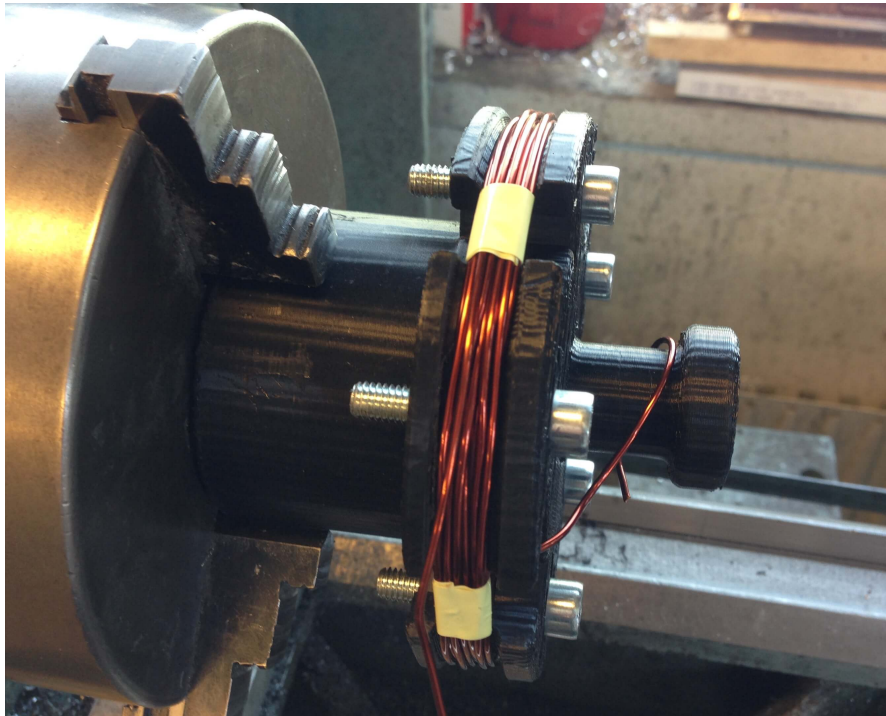
Figure 4.8: *Jig used to produce the windings*
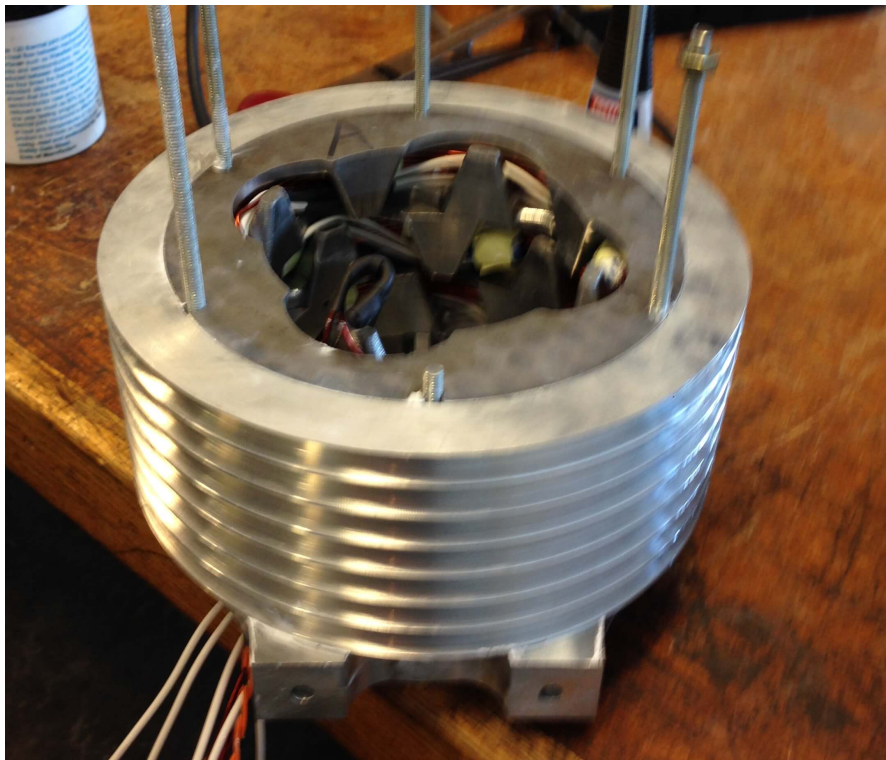
Figure 4.9: *Assembly of the complete stator with cooling mantle*

Figure 4.10: *Inside of the winded stator, where the the thermal switches can be seen as white/blue component taped to the winding*

5 Measurements on prototype machine

The phase resistance was measured to 74.8 mΩ. The average self-inductance was 195 µH, the varying inductance was measured to be 102 µH and the mutual inductance between phases was measured and approximated to 48 µH. Ψ_m was measured to 0.021 V/Hz. These parameters were then transformed over to the dq-domain using the method explained in section 2.1 and the resulting values can be seen in Table 5.1.

Table 5.1: measured value in the dq-domain

R_s	74.8 mΩ
L_{sd}	348 µH
L_{sq}	42 µH
Ψ_m	0.021 V/Hz

Since the equivalent parameters have been measured, the dq-voltages and dq-currents can be calculated in the same way as with the simulated values, using (2.19). By setting the maximum absolute voltage to 48 V and the current angle equal to the MTPA angle shown in Figure 5.1.
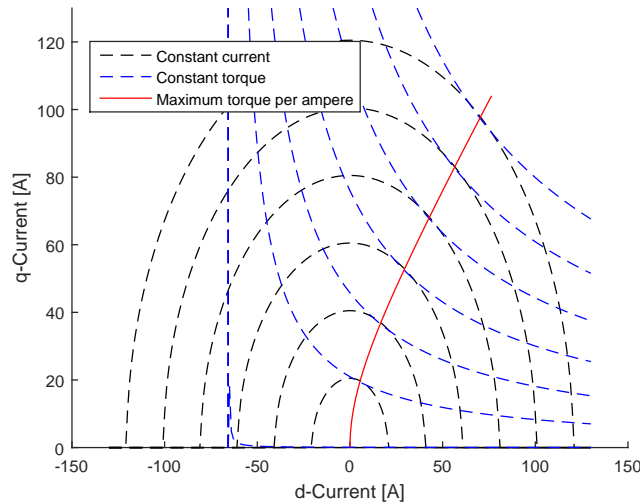

Figure 5.1: *Visualisation of the field enhancement curve for maximum torque per ampere*

5.1 Nominal torque

For the measured nominal torque the nominal current is 20 A and the current speed characterisics can be seen in Figure 5.2, where the dq-components contributions is calculated using the MTPA angle from Figure 5.1. The voltage speed characteristics with dq-components can be seen in Figure 5.3 and the absolute voltage and current are plotted agains speed together in Figure 5.4.
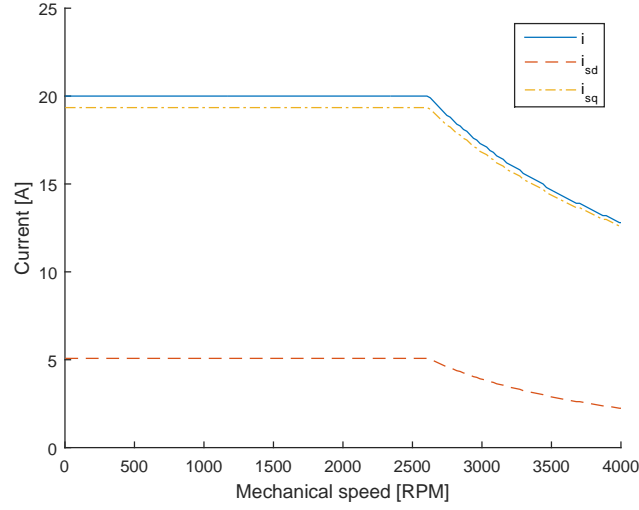
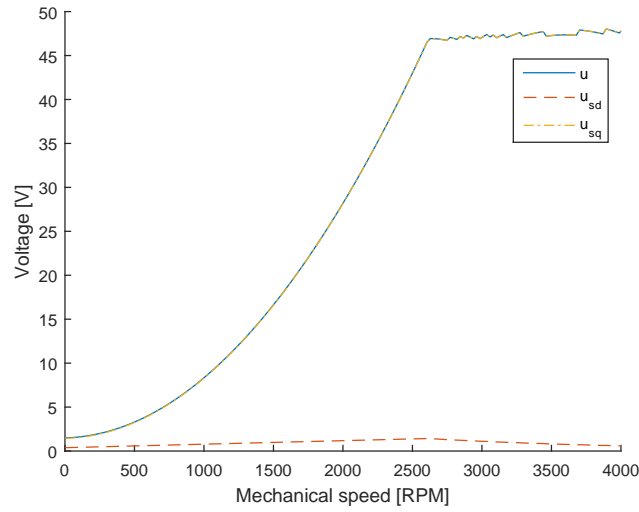Figure 5.2: *Current components speed characteristics for MTPA from measured values*

Figure 5.3: *The voltage components speed characteristics for MTPA calculated from measured values*
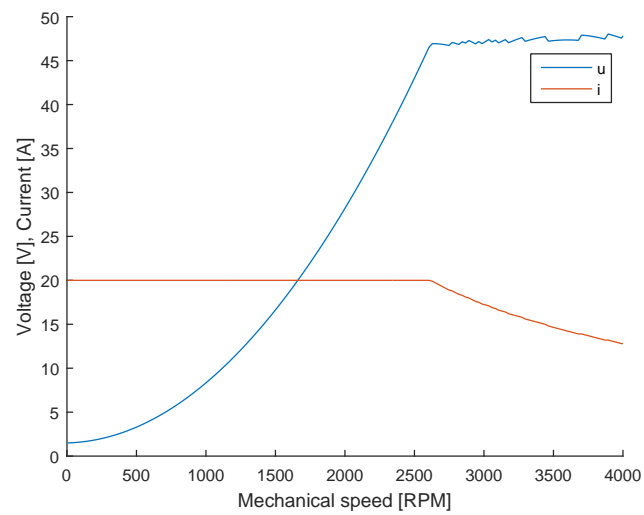
Figure 5.4: *Voltage and current per speed characteristics calculated from measured values*

The nominal electrical torque is then calculated using (2.21), the magnetic torque component with (2.22) and the reluctance torque component by using (2.23). These torque contributions is then plotted against the mechanical speed and is shown in Figure 5.5. The nominal power at different speeds can be seen in Figure 5.6
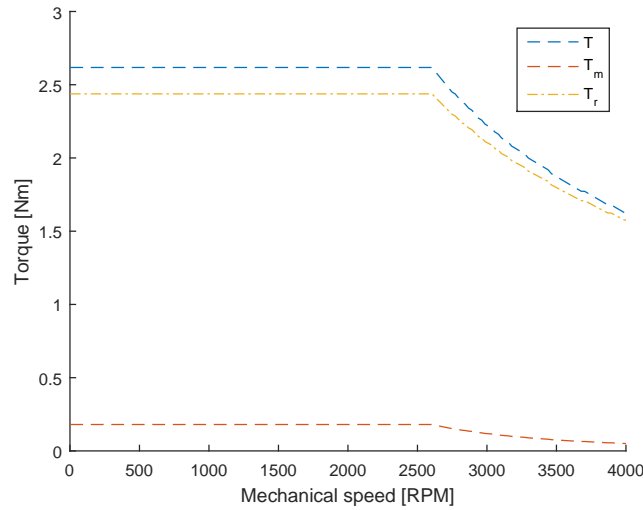

Figure 5.5: *Nominal torque components at different speed calculated from measured values*
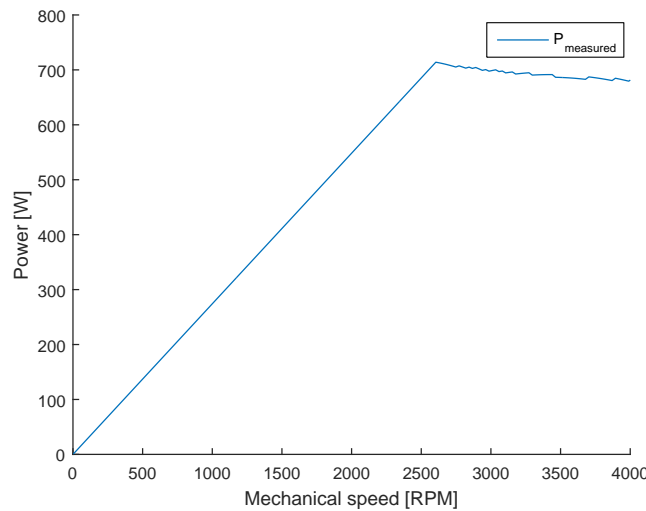

Figure 5.6: *Nominal power at different speed calculated from measured values*

5.2 Peak torque

For the peak torque the maximum current is 100 A. The current speed characteristics with dq-component is shown in Figure 5.7, where the current angle is calculated from the MTPA shown in Figure 5.1. The voltage speed characteristics with dq-compnent contribution is shown

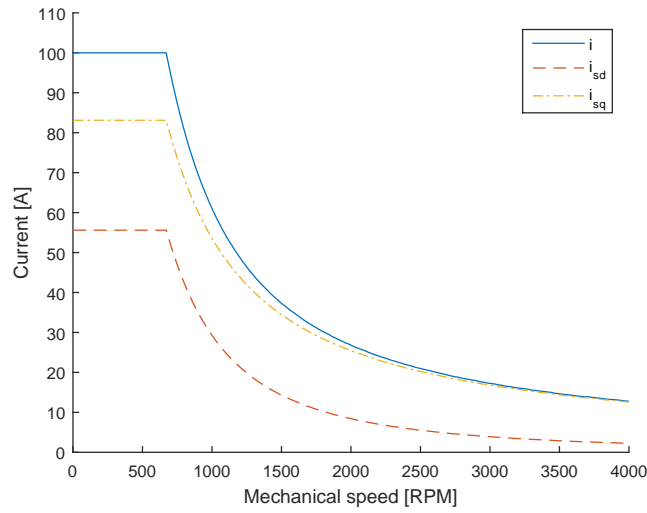in Figure 5.8. The absolute voltage and current is then plotted against speed in Figure 5.9

Figure 5.7: *Maximum current components speed characteristics for MTPA from measured values*
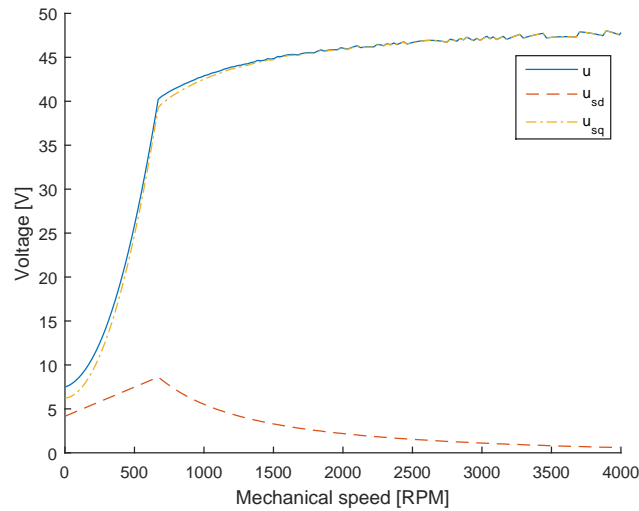

Figure 5.8: *The voltage components speed characteristics for MTPA calculated from measured values*

The electrical torque is then calculated using (2.21), the magnetic torque component with (2.22) and the reluctance torque component by using (2.23). These torque contributions is then plotted against the mechanical speed and is shown in Figure 5.10. The maximum power at different speeds can be seen in Figure 5.11
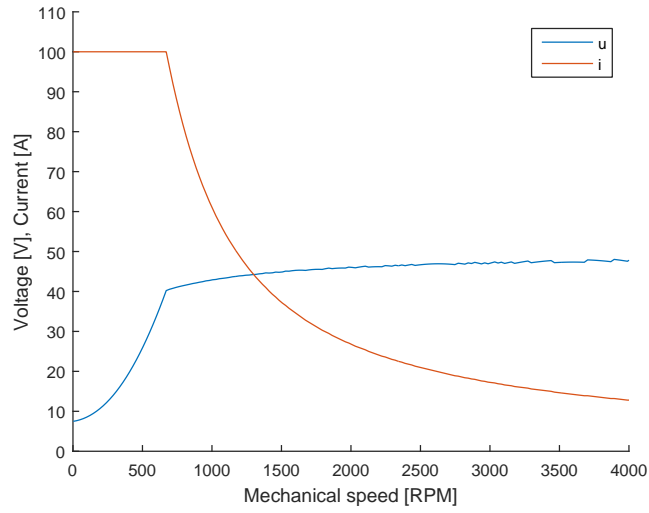
Figure 5.9: *Voltage and current per speed characteristics calculated from measured values*
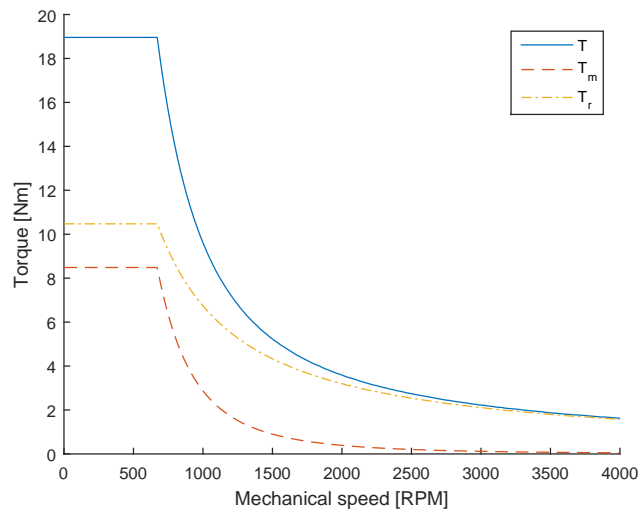

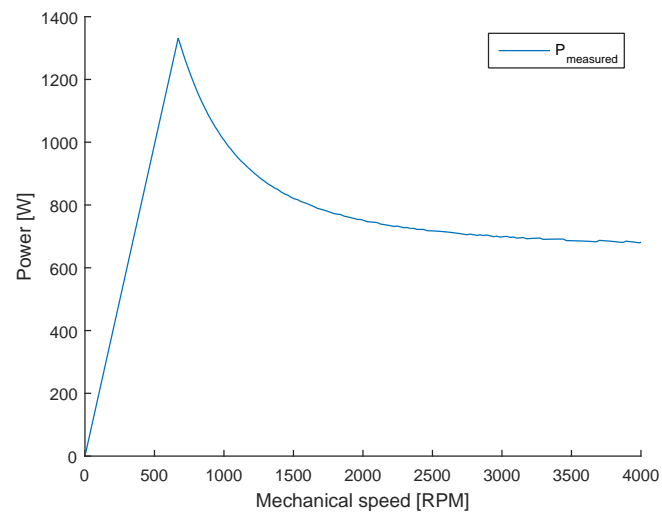Figure 5.10: *Maximum torque components at different speed calculated from measured values*

Figure 5.11: *Maximum power at different speed calculated from measured values*

6 Analysis

In this section the comparison between the FE-calculated parameters and the measured parameters is done. The FE-calculated and the measured parameter values are shown in Table 6.1. The FE-calculated winding resistance was calculated on the active part of the coil winding, while the measured winding resistance was measured at the end terminal of the winding. Both the FE-calculation and the measurements was done at room temperature. The amount of extra length of the wire in the winding is approximated to be around 30 mm per phase which corresponds to approximately 4.5 mΩ. The difference in the dq-inductances comes from a difference of around 5% at the average self-inductance and the varying inductance, and that the FE-calculated mutual inductance was approximated to 0.

Table 6.1: FE-calculated and measured value in the dq-domain

	FE-calculated value	measured value
$L_{average}$	207.5 μH	195 μH
$L_{varying}$	97.5 μH	102 μH
L_{mutual}	0 μH	48 μH
R_s	62.5 mΩ	74.8 mΩ
L_{sd}	354 μH	348 μH
L_{sq}	61 μH	42 μH
Ψ_m	0.0206 V/Hz	0.021 V/Hz

The phase angle for MTPA is the same for both the FE-calculated and the measured values, this can be seen in Figure 6.1 where the MTPA lines overlay each other.
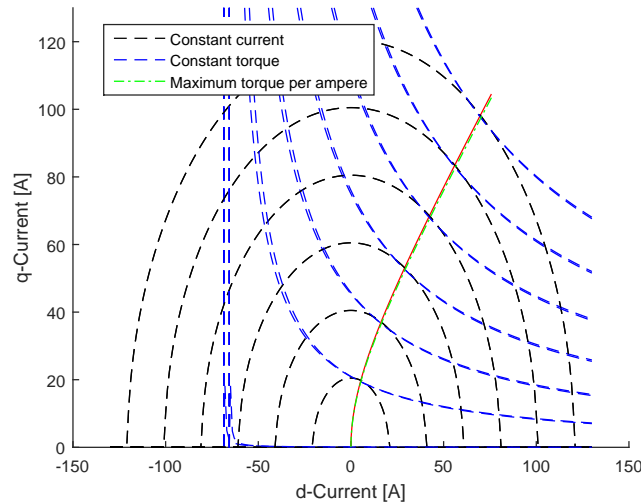

Figure 6.1: *Visualisation of the field enhancement curve for maximum torque per ampere for FE-calculated and measured cases*

6.1 Nominal torque

Comparison with the applied voltage at different speeds for nominal load torque can be seen in Figure 6.2. The difference between the FE-calculated and the measured torque speed characteristics is shown in Figure 6.3. It can be seen that the measured case have a higher torque, this seems to be from that the difference between L_{sd} and L_{sq} and that Ψ_m is larger in the measured case. The measured and FE-calculated power speed curves can be seen in Figure 6.4.
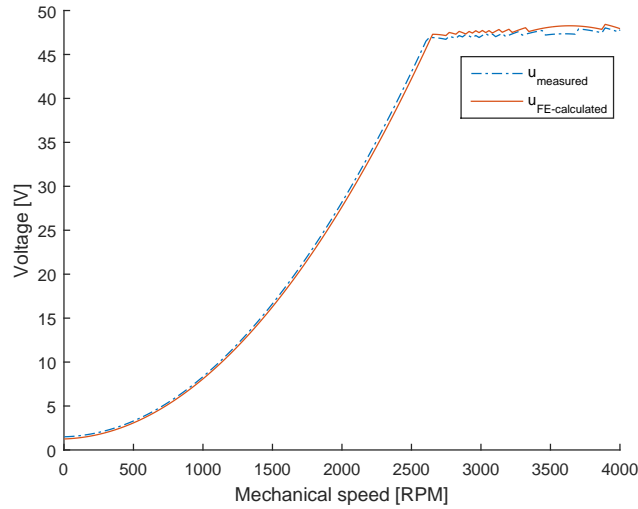

Figure 6.2: *Comparison between the FE-calculated and the measured voltage speed characteristics*
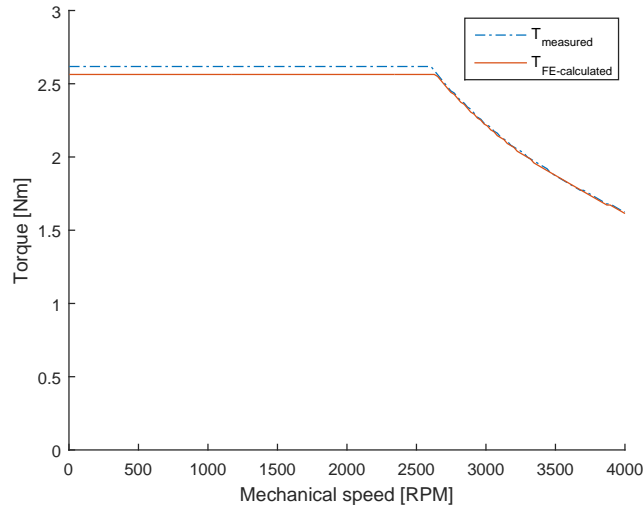

Figure 6.3: *Comparison between the FE-calculated and the measured maximum torque speed characteristics*
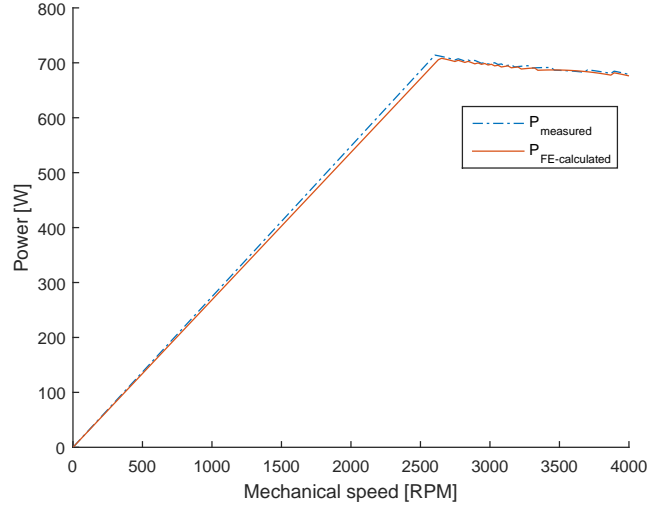
Figure 6.4: *Comparison between the FE-calculated and the measured maximum power speed characteristics*

6.2   Peak torque

The applied voltage at different speeds for maximum load torque can be seen in Figure 6.5. It can be seen that at lower speed the measured voltage is higher which is explained with that the winding resistance is higher in the measured case. While in higher speeds the FE-calculated case demands higher voltage which is explained by that the inductance in higher in the FE-calculated case.
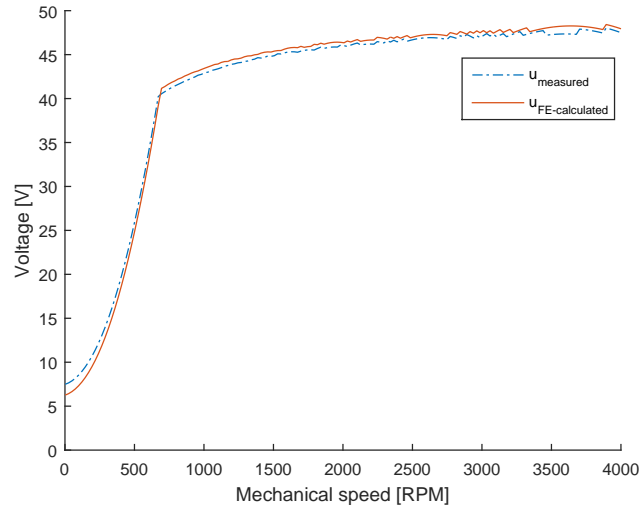

Figure 6.5: *Comparison between the FE-calculated and the measured voltage speed characteristics*

The same characteristic difference between the FE-calculated and the measured torque speed characteristics can be seen in Figure 6.6. The measured and FE-calculated power speed curves can be seen in Figure 6.7.
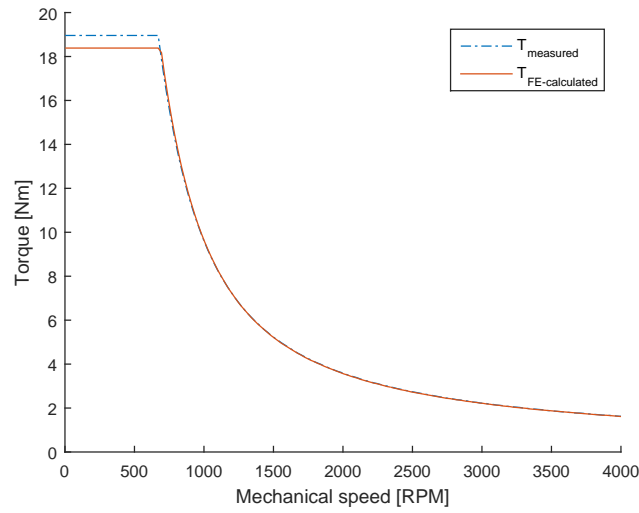
Figure 6.6: *Comparison between the FE-calculated and the measured maximum torque speed characteristics*
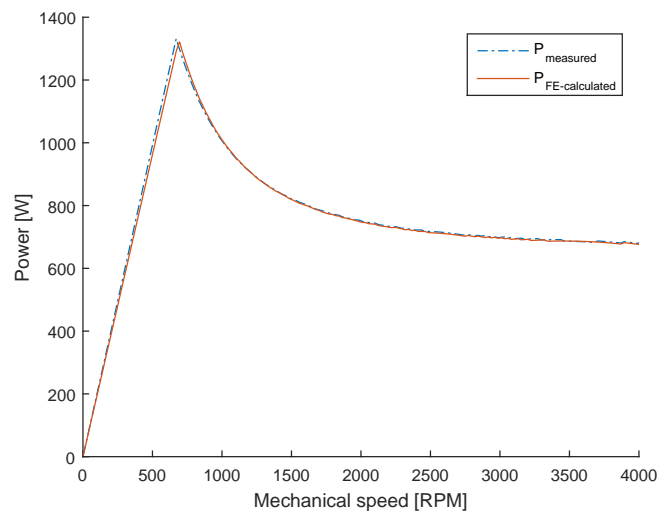

Figure 6.7: *Comparison between the FE-calculated and the measured maximum power speed characteristics*

7 Conclusion

A claw pole machine with a nominal power of 708 W and a peak power of 1300 W with a peak torque of 19 Nm, has been designed, built and verified through measurements. The equivalent circuit parameters was calculated to $R_s = 62.5\ m\Omega$, $L_{sd} = 354\ \mu H$, $L_{sq} = 61\ \mu H$ and $\Psi_m = 0.0206$ while the measured equivalent parameters is $R_s = 74.8\ m\Omega$, $L_{sd} = 348\ \mu H$, $L_{sq} = 42\ \mu H$ and $\Psi_m = 0.021$. The amount of hard magnetic material in the machine is 44 g and the reluctance torque in the machine was used as the primary generation of torque at nominal load. While at peak torque operation the magnetic torque contribution was significantly higher.

This work has shown that it is possible to prototype electrical machines using milling and turning using Somaloy Prototyping Material. Even if some difficulties exist, machining the material it is still a viable prototyping method. This could give small businesses a possibility to design and prototype electrical machines without investing in specially built machinery and tooling otherwise necessary.

Bibliography

[1] J. Paul, "Investigating rare earth element mine development in epa region 8 and potential environmental impacts." EPA Document-908R11003, August 2011.

[2] E. Alonso, A. M. Sherman, T. J. Wallington, M. P. Everson, F. R. Field, R. Roth, and R. E. Kirchain, "Evaluating rare earth element availability: A case with revolutionary demand from clean technologies," *Environ Sci Technol.*, vol. 46, no. 8, pp. 4684–4684, 2012.

[3] Y. Suzhu, M. Zardinejad, J. Wei, W. Zhou, S. Subbiah, Z. Hongyu, P. Ji, Z. W. Xu, Fengzhou, H. Hocheng, H.-Y. Tsai, G. Yang, D. S. K. Wong, G. Qi, S. Z. Shanyong, B. Song, and M. K. Tiwari, *Handbook of manufacturing engineering and technology.* Springer, 2015.

[4] S. Lundmark, *Application of 3-D Computation of Magnetic Fields to the Design of Claw-Pole Motors.* Doktorsavhandlingar vid Chalmers tekniska hgskola. Ny serie, no: 2313, Institutionen för energi och milj, Elteknik, Chalmers tekniska hgskola,, 2005. 118.

[5] L. O. Hultman and A. G. Jack, "Soft magnetic composites-materials and applications," *Electric Machines and Drives Conference*, vol. 1, pp. 516–522, 2003.

[6] H. Shokrollahi and K. Janghorban, "Soft magnetic composite materials (smcs)," *Journal of Materials Processing Technology*, vol. 189, no. 13, pp. 1 – 12, 2007.

[7] A. Balakrishnan, W. T. Joines, and T. G. Wilson, "Air-gap reluctance and inductance calculations for magnetic circuits using a schwarz-christoffel transformation," *IEEE Transactions on Power electronics*, vol. 12, p. 654 to 663, July 1997.

[8] E. N. H. Hembach, D. Gerling, "Analytical design of a claw-pole motor for electrical water pump applications,"

Appendices

Höganäs 凵
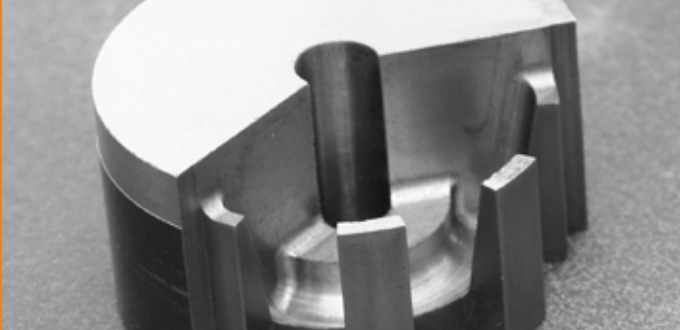
Somaloy® Prototyping Material

Quick and cheap with prototyping

Tooling is the preferred approach to manufacture prototype components with Somaloy material. Using this method, the prototyped component will in all essential respects have the same properties as a mass produced component.

A simplified approach is to machine the component from a pre-fabricated blank. This can be a fast, low-cost approach, but it also has the drawback that the properties will in most cases be different from those obtained by compaction. A special Somaloy Prototyping Material with enhanced machinability has now been developed in order to minimise these differences.

Somaloy Prototyping Material blanks exhibit stable mechanical properties up to 150ºC.

For more information, please contact your local sales representative.

To manufacture prototype components for soft magnetic applications, the blanks should be machined using conventional machining techniques (milling, turning, drilling). Non conventional machining (such as electro discharge machining, EDM) would deteriorate the material and therefore should be avoided. Design with walls thinner than 2 mm should be avoided.

In order to machine larger components, Somaloy Prototyping Material blanks can be cut and glued together (epoxy glue) before machining.


www.hoganas.com/somaloy
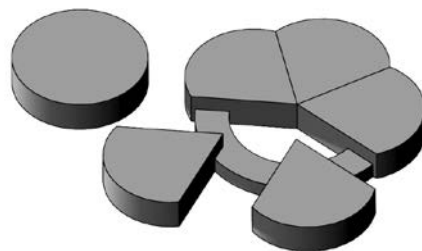
Typical Data and Machining Recommendations

|		Somaloy Prototyping Material		
		Diameter 80 mm Height 20 mm	Diameter 80 mm Height 40 mm	Diameter 120 mm Height 20 mm
Density [g/cc]		7.45	7.30	7.30
TRS @ ambient [MPa]		60	60	60
Resistivity [$\mu\Omega$.m]		280	280	260
B_{max}@4000 A/m [T]		1.26	1.19	1.23
B_{max}@10000 A/m [T]		1.53	1.46	1.49
H_c [A/m]		200	200	210
μ_{max}		455	430	435
Core losses @ 1T [W/kg]	50 Hz	5	5	5
	200 Hz	21	22	22
	400 Hz	46	48	49
	600 Hz	74	79	79
	800 Hz	104	111	111
	1000 Hz	138	147	147

All properties are measured on toroids (OD55 ID45 H5 mm) machined from the different Somaloy Prototyping Material blanks.

Here are some recommendations on tooling and process parameters for machining Somaloy® Prototyping Material.
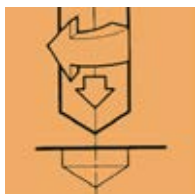
DRILLING

- HSS self-centering drill
- Cutting speed: V_c = 30 m/min
- Feed speed: V_f = 60 mm/min
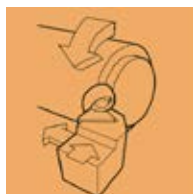
TURNING

- Cermet-polished sharp inserts, for machining of aluminium and plastic materials
- Cutting speed: V_c in the range 50-300 m/min
- Feed: f = 0.12 mm/rev recommended for a good surface finish
- Cutting fluid can be used for better machinability
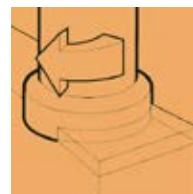
MILLING

- Super sharp carbide milling cutter, for machining of aluminum and plastic materials
- Cutting speed: V_c in the range 100-125 m/min
- Feed per tooth: f_z = 0.05 mm/tooth

VACOMAX 225 HR

Permanent magnets with high remanence and the highest temperature stability attainable from rare-earth materials. Use at temperatures up to 350 °C is possible (e.g. clutches).

Magnetic properties

Remanence		Coercivity			Energy density		Temperature coefficient (RT - 100 °C)		Temperature coefficient (RT - 150 °C)	
B_r typ. T	B_r min. T	H_{cB} typ. kA/m	H_{cB} min. kA/m	HcJ min. kA/m	$(BH)_{max}$ typ. kJ/m^3	$(BH)_{max}$ min. kJ/m^3	TC (B_r) %/°C	TC (H_{cJ}) %/°C	TC (B_r) %/°C	TC(H_{cJ}) %/°C
1.10	1.03	820	720	1590	225	190	-0.030	-0.18	-0.035	-0.19

Inner Magnetizing Field Strength	
$H_{mag\ min}$	
kA/m	kOe
3650	46

**Characteristic physical properties at room temperature**

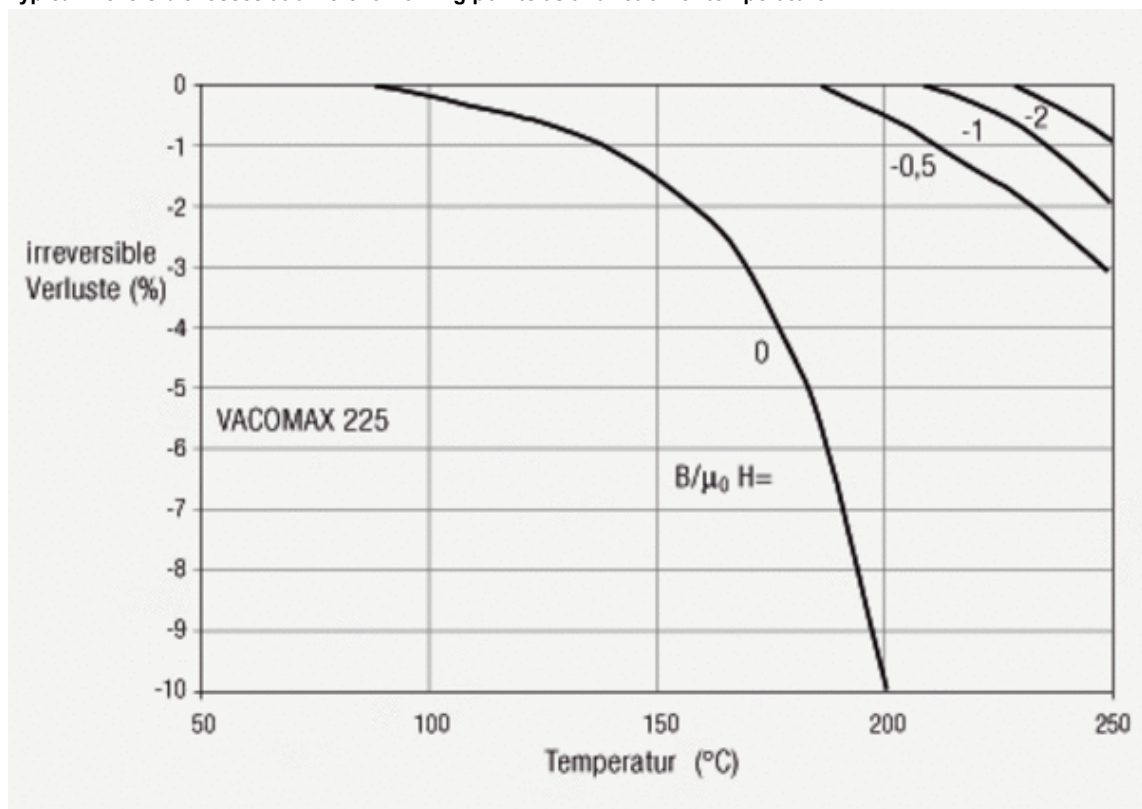| Curie temperature	Specific electric resistance	Specific heat	Thermal conductivity	Coefficient of thermal expansion 20-100 °C		Young's modulus	Bending strength	Compressive strength	Vickers hardness	Stress crack resist
°C	Ωmm^2/m	J/(kg·K)	W (m· K)	II c*) 10^{-6}/K	⊥c*) 10^{-6}/K	kN/mm^2	N/mm^2	N/mm^2	HV	K_{IC} N/mm
800-850	0.65-0.95	300-500	5-15	8-12	10-14	140-170	80-150	400-900	550-750	30-60

*) II c: parallel to preferred magnetic direction
⊥ c: perpendicular to preferred magnetic direction

Typical demagnetization curves B(H) and J(H) at different temperatures

kG   T   B/µo H ———————▶
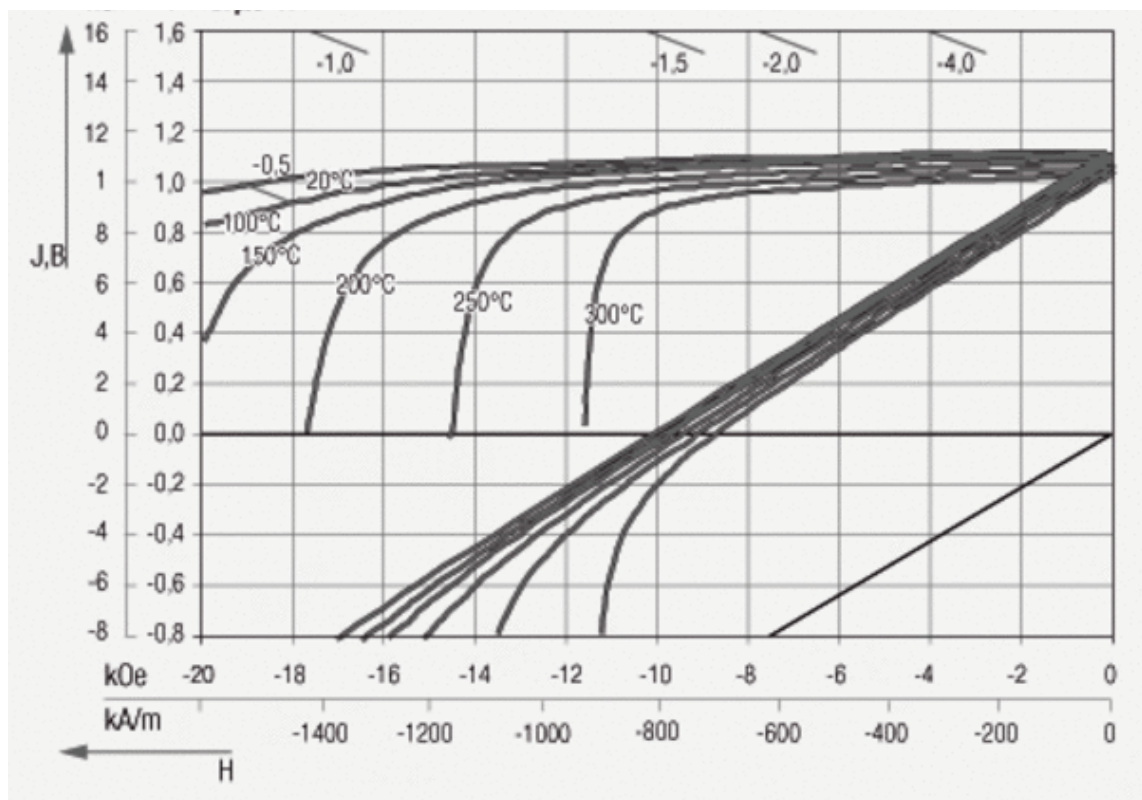
Typical irreversible losses at different working points as a function of temperature